Title

Using an Inverse Model to Reconcile Differences in Simulated and Observed Global Ethane Concentrations and Trends Between 2008 and 2014

Journal

Journal of Geophysical Research: Atmospheres, 123(19)

ISSN

2169-897X

Authors

Monks, SA
Wilson, C
Emmons, LK
et al.

Publication Date

2018-10-16

DOI

10.1029/2017jd028112

Journal of Geophysical Research: Atmospheres

RESEARCH ARTICLE
10.1029/2017JD028112

Using an Inverse Model to Reconcile Differences in Simulated and Observed Global Ethane Concentrations and Trends Between 2008 and 2014

S. A. Monks[1,2], C. Wilson[3,4], L. K. Emmons[5], J. W. Hannigan[5], D. Helmig[6], N. J. Blake[7], and D. R. Blake[7]

[1]CIRES, University of Colorado Boulder, Boulder, CO, USA, [2]Chemical Sciences Division, NOAA, Earth System Research Laboratory, Boulder, CO, USA, [3]National Centre for Earth Observation, University of Leeds, Leeds, UK, [4]School of Earth and Environment, University of Leeds, Leeds, UK, [5]National Center for Atmospheric Research, Boulder, CO, USA, [6]Institute of Arctic and Alpine Research, University of Colorado Boulder, Boulder, CO, USA, [7]Department of Chemistry, University of California, Irvine, CA, USA

Key Points:
- Inverse modeling improves global simulations of ethane by increasing global annual 2008 ethane emissions from ~7 to ~15 Tg/year
- The largest negative biases in baseline 2008 emissions were found in North America and Eurasia
- A positive trend in North American emissions between 2008 and 2014 likely explains observed increases in NH ethane

Supporting Information:
- Supporting Information S1

Correspondence to:
S. A. Monks and C. Wilson,
sarah.monks@noaa.gov;
c.wilson@leeds.ac.uk

Citation:
Monks, S. A., Wilson, C., Emmons, L. K., Hannigan, J. W., Helmig, D., Blake, N. J., & Blake, D. R. (2018). Using an inverse model to reconcile differences in simulated and observed global ethane concentrations and trends between 2008 and 2014. *Journal of Geophysical Research: Atmospheres*, *123*, 11,262–11,282. https://doi.org/10.1029/2017JD028112

Received 24 NOV 2017
Accepted 7 AUG 2018
Accepted article online 17 AUG 2018
Published online 8 OCT 2018

Abstract We use a global model, TOMCAT, and an inverse model, INVICAT, to estimate emissions of ethane (C_2H_6) between 2008 and 2014 by assimilating surface flask observations. We find that baseline global emissions in 2008 need to increase by a factor of 2.04–2.11 in order for the model to capture C_2H_6 observations, indicating large biases in current emission inventories. Most of this increase occurs over North America and Eurasia, with temperate North American emissions accounting for 23–26% of the total global emission increase and temperate Eurasian emissions accounting for 35–37%. Further to this, recent peer-reviewed analysis of long-term observational records shows an increase in C_2H_6 in the Northern Hemisphere since ~2009. Our results indicate that annual global emissions of C_2H_6 have increased at a rate of 0.27 ± 0.54–0.33 ± 0.44 Tg/yr^2 between 2008 and 2014. A statistically significant positive trend of 0.20 ± 0.11–0.24 ± 0.13 Tg/yr^2 ($p \leq 0.01$) is found in temperate North America, resulting in emissions that are 31–32% larger in 2014 than in 2008. Our results corroborate previous studies' conclusions that a rapid increase in oil and natural gas production in United States over this time period is likely a large driver of the change in emissions.

1. Introduction

Ethane (C_2H_6) is the most abundant nonmethane hydrocarbon (NMHC) in the troposphere (partly due to its relatively long lifetime of 2 months) and plays an important role in atmospheric chemistry (Blake & Rowland, 1986). In the presence of nitrogen oxides (NO_x), emissions of C_2H_6 can result in the production of ozone (O_3). O_3 is detrimental to human health (Bell et al., 2004; Brunekreef & Holgate, 2002), can decrease crop yields (Van Dingenen et al., 2009), and has a positive (warming) radiative effect on the climate (e.g., Myhre et al., 2013; Sitch et al., 2007). C_2H_6 oxidation is also a large source of acetaldehyde (CH_3CHO; Millet et al., 2010), which can lead to the formation of peroxy acetyl nitrate (PAN), a reservoir species of NO_x (Fischer et al., 2014). The intercontinental transport of PAN provides a source of NO_x in regions away from emissions, where it can contribute to O_3 production (Hudman et al., 2004; Singh, 1987). Further to this, tropospheric loss of C_2H_6 from the atmosphere is predominantly through reaction with the hydroxyl radical (OH; Rudolph & Ehhalt, 1981), a chemical compound that controls the residence time of most pollutants in the troposphere (Ehhalt et al., 1990). Therefore, C_2H_6 emissions can reduce the oxidative capacity of the atmosphere and indirectly affect the climate by extending the lifetime of methane (CH_4), a greenhouse gas with a global warming potential that is higher than that of CO_2 (Collins et al., 2002).

C_2H_6 is primarily emitted during the production of oil and natural gas (O&NG), resulting in a strong interhemispheric gradient, with the largest concentrations co-located with anthropogenic activities in the Northern Hemisphere (NH; Rudolph, 1995; Xiao et al., 2008). Other smaller sources include biomass burning, biogenic, and oceanic (Xiao et al., 2008). Annual average background mixing ratios were 1049 ± 99 ppt in the NH and 277 ± 34 ppt in the Southern Hemisphere (SH) between 1984 and 2010 (Simpson et al., 2012). Recent studies have highlighted that the current generation of chemistry models underestimate observed C_2H_6 in the mid-to-high northern latitudes (Emmons et al., 2015; Franco et al., 2016; Tilmes et al., 2016; Monks et al., 2017;

Dalsøren et al., 2018). Pétron et al. (2014) used observations affected by U.S. O&NG emissions to show that a regional emission inventory underestimated total NMHC emissions by around a factor of 2 in Colorado in 2012. Franco et al. (2016) found that they needed to double anthropogenic C_2H_6 emissions in a global model to match observed total column concentrations over North America and Europe in 2007. Tzompa-Sosa et al. (2017) found that they needed to increase C_2H_6 emissions from the 2011 regional National Emission Inventory (NEI) by 1.4 over the United States to match regional aircraft and surface observations. These studies indicate that current emission inventories underestimate emissions of C_2H_6, and possibly other NMHCs. Given the importance of C_2H_6 in atmospheric chemistry, it is essential to understand these global emission biases.

In addition to this, C_2H_6 observations exhibit long-term changes in concentrations that are likely to reflect changes in emissions. Global surface data analyzed between 1984 and 2010 showed a decrease in concentrations of ~7 ppt/year (Simpson et al., 2012). However, surface and total column measurements in the NH now show a reversal of this negative trend beginning around 2009, with some surface sites showing positive trends of $>$50 ppt/year in the United States (Franco et al., 2015; Franco et al., 2016; Hakola & Hellén, 2016; Hausmann et al., 2016; Helmig et al., 2016). The recent positive trend in C_2H_6 occurred during a period that has seen a rapid increase in US O&NG production (Kort et al., 2016; Peischl et al., 2016). As a result, it has been proposed that the United States is a major driver of the recent observed changes in C_2H_6 concentrations (Franco et al., 2016; Kort et al., 2016). This is further supported by measurements made since 2010 that show an increase in C_2H_6 concentrations in air originating from regions with active O&NG wells (Vinciguerra et al., 2015). In particular, increased O&NG production in the Bakken Formation of western North Dakota alone has been estimated to contribute an annual growth rate of 0.06 Tg/yr^2 to global ethane emissions (Kort et al., 2016).

Inverse modeling is one method that has become increasingly employed over recent years to estimate trace gas emissions on aregional and global scales (e.g., Alexe et al., 2015; Babenhauserheide et al., 2015; Fraser et al., 2013; Gurney et al., 2003; Thompson et al., 2014). This statistical technique minimizes model-observation differences through adjustments to model parameters (e.g., emissions), producing posterior parameter estimates that are consistent with the observations. C_2H_6 has a relatively long lifetime of a few months compared to other reactive NMHCs (Rudolph, 1995), allowing it to undergo intercontinental transport. This means that measurements of C_2H_6 can reflect nonlocal changes in emissions and chemistry (e.g., changes in OH), and can be assimilated into an inverse model to estimate regional and global emissions and provide some insight into model C_2H_6 simulation biases. In addition to this, C_2H_6 is one of only a few NMHCs that are monitored within an extensive long-term global monitoring network (Helmig et al., 2014; Schultz et al., 2015). An inverse modeling study that covers a period from 2009 onward could indicate where emissions are likely to have changed in order to have caused the positive trend in observed C_2H_6 concentrations in the NH.

Inverse studies of global anthropogenic C_2H_6 emissions for a single year have been published previously (Franco et al., 2016; Tzompa-Sosa et al., 2017; Xiao et al., 2004; Xiao et al., 2008). However, these were done indirectly, mostly through the use of CH_4 fossil fuel emission estimates and observationally derived methane-to-ethane emission ratios (MERs). This method introduces a significant amount of uncertainty as MERs vary significantly between regions (e.g., Helmig et al., 2016), and there are difficulties in accurately separating O&NG CH_4 emissions from other sources as they are often co-located (Franco et al., 2016). For this reason, it is preferable to directly estimate C_2H_6 emissions using an inverse model simulation of C_2H_6 and C_2H_6 observations.

In this study, we provide the first global inverse modeling estimate of C_2H_6 emissions using observations of C_2H_6 instead of CH_4. We use the global chemical transport model (CTM), TOMCAT, along with its adjoint, ATOMCAT, and the variational inverse model, INVICAT, to estimate global emissions of C_2H_6 between 2008 and 2014. This allows us to investigate baseline emission biases in 2008 and trends in emissions over this seven-year period. We have three main aims: (1) estimate where, and by how much, baseline (2008) emissions need to change in order remove the current large biases in simulated C_2H_6 that are a common feature in chemistry models; (2) investigate the impacts of this common emission bias on tropospheric chemistry; and (3) estimate regional emissions trends that can explain recent observed increases in NH atmospheric C_2H_6.

The models used in this study are described in sections 2.1 and 2.2. Surface flask measurements of C_2H_6 that are assimilated into the inverse model are described in section 2.3. The a priori emissions used in these models are described in section 2.4. The independent data used to evaluate the a posteriori emissions produced by the inverse model are described in section 2.6. We discuss the modeling results relating to the 2008 baseline emissions in section 3.1, evaluate the a posteriori emissions in section 3.2, and consider the effect of changes in the baseline emissions on atmospheric tropospheric chemistry in section 3.3. The derived 2009–2014 trends in C_2H_6 emissions are discussed in section 3.4, and trends in simulated C_2H_6 concentrations are discussed in section 3.5.

2. Modeling Methods and Observational Data

2.1. TOMCAT Model Description

TOMCAT is a three-dimensional Eulerian CTM that has been used in several global tropospheric chemistry studies (e.g., Monks et al., 2015; Pope et al., 2016; Rap et al., 2015; Richards et al., 2013; Scott et al., 2018). Model dynamical processes, such as tracer advection, boundary layer mixing, and convection, are described by Chipperfield (2006). The model is forced using meteorological data from the European Centre for Medium-Range Weather Forecasts ERA-Interim analyses (Dee et al., 2011). Model simulations that are used to evaluate C_2H_6 emission data sets employ a simplified chemistry scheme using off-line OH concentrations and are described in section 2.1.1. The impacts of emission biases on atmospheric chemistry are investigated using the full chemistry version of the model, which is described in section 2.1.2.

2.1.1. Simplified Chemistry Scheme

The tropospheric chemistry of C_2H_6 is relatively simple with no secondary production in the atmosphere. After emission, the primary route for loss from the atmosphere is by reaction with OH. This allows us to simulate tropospheric C_2H_6 concentrations using a simplified model chemistry scheme, where prescribed monthly mean OH concentrations are used to diagnose loss rates. Simplified chemistry schemes have been used previously in TOMCAT for CO and CH_4, and have been shown to perform well against observations (Monks et al., 2012; Wilson et al., 2016). For C_2H_6, the chemical loss is calculated according to the kinetics of C_2H_6 + OH ($k = 7.66 \times 10^{-12} e^{(-1020/T)}$; Sander et al., 2011). Large intermodel OH differences highlight the uncertainties that exist in simulated global tropospheric OH in current state-of-the-art CTMs (e.g., Emmons et al., 2015; Monks et al., 2015; Voulgarakis et al., 2013). This means that emission estimates derived from model inversions using OH calculated online are model dependent (e.g., Franco et al., 2016; Tzompa-Sosa et al., 2017). For this reason, we have chosen to use monthly-varying OH taken from Patra et al. (2011). This OH data set is from Spivakovsky et al. (2000), which is constrained by observations of methyl chloroform, with an 8% decrease applied globally to reflect more recent observations (Huijnen et al., 2010). This data set is thought to give a reasonable representation of the distribution and magnitude of OH in the troposphere (e.g., Patra et al., 2011), and removes any existing model biases in OH. There have been previous comparisons between observed methyl chloroform and the equivalent simulated in TOMCAT using these OH fields (McNorton et al., 2016; Patra et al., 2011), in which the model simulations matched observed MCF to a high level of accuracy. It is worth noting that our method does not account for year-to-year variability in OH, which may have some effect on our results, even though this variability is believed to be small (Montzka et al., 2011). Reactions of C_2H_6 with bromine and chlorine are also not included in the model, which may cause our results to underestimate the magnitude of C_2H_6 emissions. These simulations are run with a horizontal resolution of 2.8° × 2.8° and 60 vertical levels extending from the surface up to 0.1 hPa and are used to evaluate the C_2H_6 emission data sets. Given the relatively short lifetime of C_2H_6, transport to the stratosphere and subsequent destruction is expected to be a small component of the total atmospheric sink.

2.1.2. Full Chemistry Scheme

The full chemistry version of TOMCAT includes a detailed tropospheric chemistry scheme with ~79 chemical species, accounting for reactions of C_2–C_{10} hydrocarbons, NO_x, HO_x, CO, O_3, and CH_4. This version of the model simulates OH online, unlike the simplified chemistry scheme, and therefore accounts for interactions with other chemical species. This version of the model also accounts for the effects of wet and dry deposition. Details and evaluation of the tropospheric chemistry scheme can be found in Monks et al. (2017). These simulations are run with a horizontal resolution of 2.8° × 2.8° and 31 vertical levels extending from the surface up to 0.1 hPa. This version of the model is used to assess the impact of C_2H_6 emission inventory biases on PAN, O_3, and CH_3CHO.

2.2. The INVICAT Model

INVICAT is an inverse atmospheric transport model based on TOMCAT, first described in Wilson et al. (2014). It employs a 4-D variational (4D-VAR) optimization framework based on Bayesian theory, similar to those described by Chevallier et al. (2005) and Meirink et al. (2008). Detailed descriptions of Bayesian inverse modeling theory can be found in the above references. Briefly, this method seeks to minimize model-observation differences by altering model parameters, while allowing for prior knowledge of these parameters to be retained. The model parameters are contained in the state vector, x, which has m elements. The optimization is obtained via a cost function, $J(x)$, which is defined as follows:

$$J(\boldsymbol{x}) = \frac{1}{2}(\boldsymbol{x} - \boldsymbol{x}_b)^T \boldsymbol{B}^{-1}(\boldsymbol{x} - \boldsymbol{x}_b) + \frac{1}{2}(\boldsymbol{y} - \boldsymbol{H}\boldsymbol{x})^T \boldsymbol{R}^{-1}(\boldsymbol{y} - \boldsymbol{H}\boldsymbol{x})$$

where x_b is the a priori estimate of x and B is the $m \times m$ error covariance matrix containing the uncertainties placed on the prior estimates, and the covariances between these uncertainties. y is a vector containing the set of n observations that are assimilated. H is the model operator, which maps x onto the observation space. R is the $n \times n$ error covariance matrix for the observations. The elements of R are made up of observational repeatability error along with model representation errors, quantifying the ability of the model and observations to between them represent the truth. R is usually diagonal.

The 4D-VAR method of inverse modeling finds the optimal value of x through iterative minimization of $J(x)$, which requires the evaluation of its gradient, defined as

$$\nabla J(\boldsymbol{x}) = \boldsymbol{B}^{-1}(\boldsymbol{x} - \boldsymbol{x}_b) + \boldsymbol{H}^T \boldsymbol{R}^{-1}(\boldsymbol{y} - \boldsymbol{H}\boldsymbol{x})$$

H^T represents the adjoint version of the tangent linear of the model operator H. In reality, the matrices H and H^T are represented by forward and adjoint transport models, along with a function that maps the simulated concentration fields to the location and time that the observations were made. ATOMCAT, the adjoint version of the TOMCAT model, is described in Wilson et al. (2014). In our case, since the transport in the TOMCAT model is linear, ATOMCAT is the exact adjoint of the forward model.

Both the forward and the adjoint simulations of each iteration of the inversions were run at 5.6° × 5.6° horizontal resolution, with 31 vertical levels up to 10 hPa. Note that, due to the large time requirements for running many iterations of the inverse model, this is a lower resolution than the forward simulations described in sections 2.1.1 and 2.1.2. For each assimilated observation, the simulated mixing ratios were linearly interpolated in space to the site location, and the model was co-sampled at the correct time. Although the resolution of the inverse model is lower than that of the forward model, it was shown in Wilson et al. (2014) that the effect of resolution on transport in TOMCAT is relatively small, and in order to produce the required number of iterations of each inversion, a low resolution was preferred. The state vector x contains the monthly-mean C_2H_6 emissions from each model grid cell, while the observation vector y is made up of atmospheric concentrations of C_2H_6 taken from observations (see section 2.3 for description). The total observational error δy_{tot} contained in the diagonal matrix R is made up of repeatability error, δy_{obs}, and model representation error, δy_{mod}. δy_{obs} is set at 3% of the measured concentration (based on C_2H_6 measurement deviations given in the "readme" files that accompanied the observational data). δy_{obs} is not permitted to be smaller than 3 ppt. δy_{mod} is evaluated as the mean difference in the simulated concentration between the model grid cell in which each observation falls and the surrounding vertical and horizontal grid cells. This accounts for the fact that model errors are larger in the vicinity of large source areas, where the largest atmospheric gradients are expected. For observations in the extratropical southern hemisphere (south of 60°S), an extra model transport error of 70 ppt is included to account for the fact that the large distance of these sites from emission regions means that they are likely to be affected by inaccuracies in the large-scale interhemispheric transport in the model. The prior emissions x_b are given uncorrelated uncertainties of 1,500% in each grid cell. When these large grid-box-scale errors are aggregated together over regional scales, they produce smaller relative errors. This value was chosen as it leads to an annual uncertainty of approximately 100% over the temperate North American region (see Figure 1a), which was suggested as the necessary change in emissions in order to match observations by Franco et al. (2016). The inversion period starts on 1 January 2007 and runs until 28 February 2015. For each year, the inversion runs for 14 months, with emission estimates for the last two

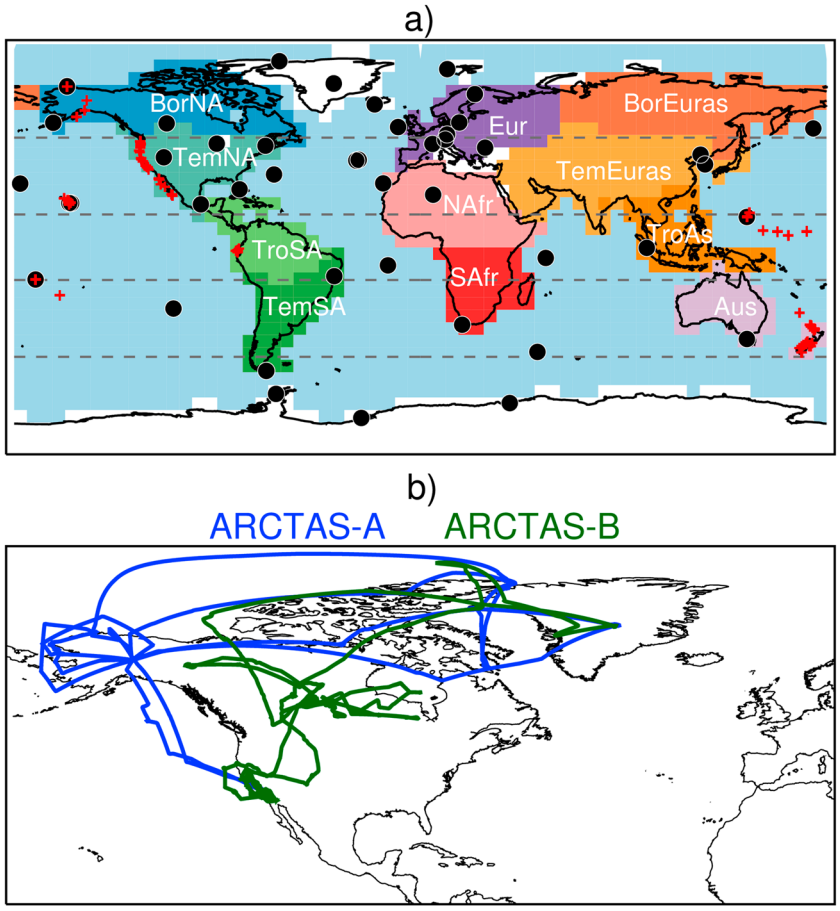

Figure 1. Maps showing (a) the locations of INSTAAR/NOAA C_2H_6 surface observations (black circles) assimilated by the INVICAT, UCI flask data collection sites (red crosses) and the regions these are binned by (gray dashed lines), and the regions over which emission changes and trends are calculated (colored regions) and (b) the flight tracks of the DC-8 during the ARCTAS-A (blue lines) and ARCTAS-B (green lines) aircraft campaigns and the location of the Jungfraujoch FTIR site. The colored regions are the following: BorNA = boreal North America, TemNA = temperate North America, Eur = Europe, BorEuras = boreal Eurasia, TemEuras = temperate Eurasia, TroSA = tropical South America, TemSA = temperate South America, NAfr = North Africa, SAfr = South Africa, TroAs = tropical Asia, and Aus = Australia.

months of each simulation being discarded. The results for the year 2007 are also discarded as spin-up. Each inversion therefore overlaps with the following inversion for two months, but is initialized using concentrations provided from the correct date in the previous inversion, so that total C_2H_6 burden is conserved across years. Each inversion was stopped after 40 iterations, which was enough for the norm of the posterior gradient of the cost function to be less than 10% of the initial gradient norm. Although this gradient norm reduction might be thought of as relatively small, it is enough to contribute to significant posterior error reductions across the most important emission regions (Figure 2). Further investigation indicates that the vast majority of the remaining contributions to the gradient norm are due to small model-observation errors in the extratropical southern hemisphere. The χ^2 statistic, which represents how well the cost function has reduced, is found by dividing the value of the cost function after the inversion is complete by the number of observations and should be close to 1 for a well-defined problem for which the minimum has been found (e.g., Chevallier et al. 2007). For each of our inversions, the final χ^2 value is between 0.8 and 2, and is generally close to 1 (see Table S1). We produce an estimate for the posterior emission covariance error matrix using the L-BFGS method (Nocedal, 1980) and updates suggested by Bousserez et al. (2015). This uses multiple iterations in order to estimate the inverse of the hessian (the second derivative) of the cost function, and does not include the off-diagonal elements of the posterior covariance matrix, so the posterior errors described in this manuscript are likely to be overestimated (Bousserez et al., 2015).

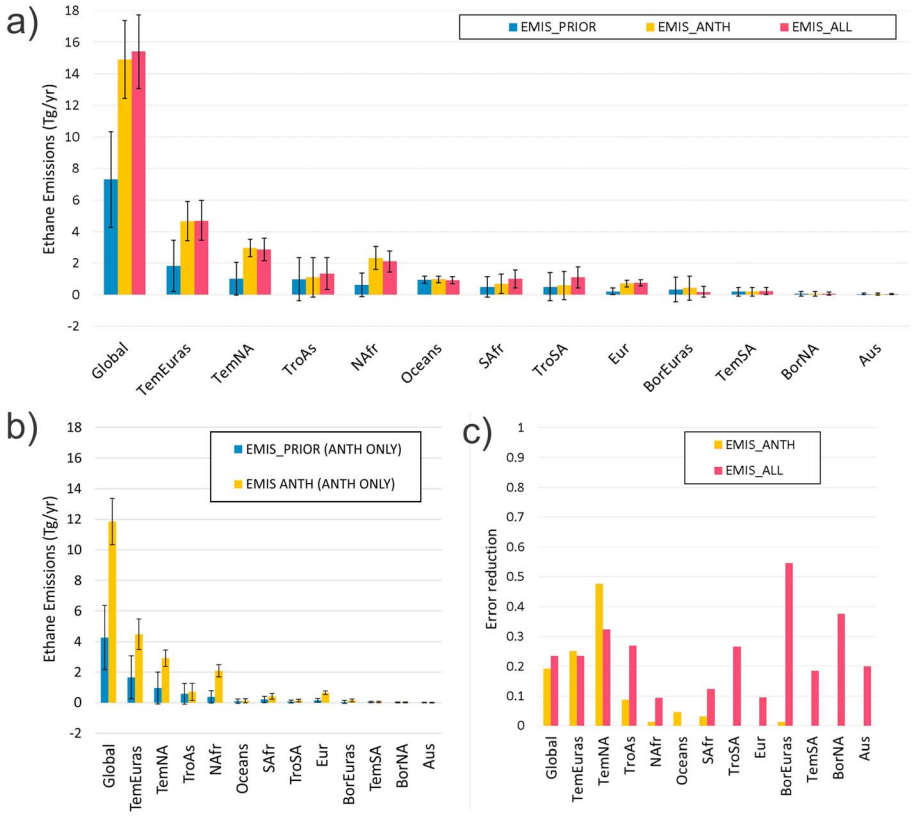

Figure 2. (a) Global and regional 2008 C_2H_6 emissions (Tg [C_2H_6]/year) from the a priori inventory (EMIS_PRIOR) and the INVICAT inverse modeling a posteriori emissions when only anthropogenic emissions are allowed to change (EMIS_ANTH) and when all emissions are allowed to change (EMIS_ALL; see Table S5 for absolute values), error bars represent the PRIOR or posterior global/regional standard deviation. (b) Same as (a) but for anthropogenic components of EMIS_PRIOR and EMIS_ANTH only. (c) Global and regional 2008 fractional error reduction for EMIS_ANTH and EMIS_ALL. See main text for description of error reduction.

2.3. Assimilated Observational Data

We use long-term surface data of C_2H_6 provided by the National Oceanic and Atmospheric Administration's Global Monitoring Division and the University of Colorado's Institute of Arctic and Alpine Research to constrain INVICAT (see Table S2). We use data from ~40 background monitoring sites, the locations of which are shown in Figure 1a. Whole air samples in flasks are collected weekly to biweekly at each site, and C_2H_6 is measured using gas chromatography with a flame ionization detection method (Pollmann et al., 2008).

2.4. A Priori C_2H_6 Emissions

The a priori emissions have been taken from widely available emission inventories. We use monthly mean anthropogenic emissions from the Representative Concentration Pathway 8.5 (which corresponds to a radiative forcing of 8.5 W/m^2 in 2100; Moss et al., 2010). This is an extension of the historical emission data set described by Lamarque et al. (2010) from the year 2000 onward and has annually varying emissions. Due to the rapid increase in U.S. O&NG production in recent years, we chose to replace this with the Environmental Protection Agency's 2011 National Emissions Inventory (NEI 2011) version 2 for the United States. This gives the model a more accurate spatial distribution of oil and gas emissions, which is important for identifying emission changes in this region using INVICAT. Anthropogenic emissions are treated as a single-source category within the model. For biomass burning, we use annually varying monthly mean emissions from the Fire INventory from NCAR (FINN v1.5; Wiedinmyer et al., 2011). Biogenic emissions are taken from the MACCity inventory (Granier et al., 2011; Lamarque et al., 2010) and were created by the Model of Emissions of Gases and Aerosol from Nature (MEGAN v2.1; Guenther et al., 2012). Ocean emissions are taken from the POET inventory and are representative of 1990 (Granier et al., 2005). It is worth noting that despite

Table 1
Summary of the C_2H_6 Emission Estimates (Including Both the A Priori and A Posteriori Data Sets) and the Chemistry Model Simulations Performed Using the Different Emission Data Sets

Name	Description
EMIS_PRIOR	A priori emissions: RCP 8.5 + NEI 2011 (v2) anthropogenic, FINN v1.5 fire, MEGAN v2.1 biogenic, POET oceanic.
EMIS_ANTH	A posteriori emissions: INVICAT allowed to change only anthropogenic emission sources.
EMIS_ALL	A posteriori emissions: INVICAT allowed to change all emission sources.
RUN_PRIOR	Simplified C_2H_6 chemistry simulation using EMIS_PRIOR.
RUN_ANTH	Simplified C_2H_6 chemistry simulation using EMIS_ANTH.
RUN_ALL	Simplified C_2H_6 chemistry simulation using EMIS_ALL.
FC_RUN_PRIOR	Full chemistry model simulation using C_2H_6 EMIS_PRIOR emissions.
FC_RUN_ALL	Full chemistry model simulation using C_2H_6 EMIS_ALL emissions.

the different emissions data sets being used to estimate the a priori global emissions, by assimilating real data and adjusting emissions in the inversion, we are partly accounting for any changes in the absolute emissions since they were constructed. However, as with all inversions, the accuracy of our final product depends to some extent on the accuracy of the prior emissions, which may be influenced by older data sets. Anthropogenic emissions are by far the biggest source of C_2H_6 (see Table S3) so most of the uncertainty will lie with the representation of these in the a priori.

2.5. Summary of Model Simulations

Table 1 summarizes the model simulations and emission data sets that are analyzed and discussed in this study. The combined emission data set used as an a priori (described in section 2.4) is referred to as EMIS_PRIOR. We perform two inverse model simulations using INVICAT, which generates two new a posteriori emission estimates that are compared to EMIS_PRIOR. In the first inversion (EMIS_ANTH), INVICAT is only allowed to change the anthropogenic emissions, assuming that the other sources are correct (biomass burning, oceanic, and biogenic). In the second inversion (EMIS_ALL), INVICAT is permitted to optimize all emission source types. In the inversions, different emission sectors are not treated separately, but are combined together within each grid cell. In order to compare with EMIS_ALL, the prior values for biomass burning, biospheric and ocean emissions are added back onto EMIS_ANTH after the inversion. The prior uncertainty due to these emissions is also included in the overall posterior error estimate for EMIS_ANTH. Using the prior error, σ_b, and the posterior error, σ_a, we define the error reduction of an inversion as $1 - \sigma_a/\sigma_b$.

To evaluate the three different emission data sets, we perform three TOMCAT forward model simulations using the simplified C_2H_6 chemistry scheme. RUN_PRIOR uses EMIS_PRIOR, RUN_ANTH uses EMIS_ANTH, and RUN_ALL uses EMIS_ALL. Finally, in order to investigate the effect of the emission biases on atmospheric chemistry, we perform two full chemistry simulations, FC_RUN_PRIOR, which uses EMIS_PRIOR, and FC_RUN_ALL, which uses EMIS_ALL. In the full chemistry runs, we are using an online chemical scheme where OH is calculated by TOMCAT. Monks et al. (2017) showed that TOMCAT OH is higher compared to the off-line OH field used by the inverse model in the lower troposphere. This will lead to a shorter lifetime of C_2H_6 in FC_RUN_PRIOR and FC_RUN_ALL and therefore a larger impact on chemistry than might occur in reality. However, as the OH field is consistent between the two full chemistry runs, the relative differences are expected to be relatively robust.

2.6. Independent Observational Data for Model Evaluation

2.6.1. ARCTAS Aircraft Data

The Arctic Research of the Composition of the Troposphere from Aircraft and Satellites (ARCTAS) campaign took place during the spring and summer of 2008 (Jacob et al., 2010). As part of this campaign, the DC-8 aircraft was based in Fairbanks, AL, from 1 to 21 April during ARCTAS-A; in Palmdale, CA, from 18 to 29 June during ARCTAS-CARB; and in Cold Lake, Canada, from 29 June to 10 July during ARCTAS-B. The ARCTAS-CARB and ARCTAS-B summer campaigns have been grouped together for this analysis and will be referred to as ARCTAS-C/B. The flights cover large parts of North America and the Arctic (Figure 1b). The air sampled was heavily influenced by anthropogenic sources originating from North America and Asia in spring, and forest

fire emissions in summer (e.g., Bian et al., 2013; Simpson et al., 2010). C_2H_6 was measured from whole air samples collected in flasks on board the DC-8 using gas chromatography (Blake et al., 2003).

2.6.2. Pacific UCI Flask Data

One of the longest records of C_2H_6 comes from whole air samples collected by the University of California, Irvine (UCI), at several remote locations in the Pacific (Blake, 2013). They give north-to-south coverage of background concentrations extending from Alaska to New Zealand. These measurements show good agreement with continuous surface measurements at other locations and are thought to be mostly representative of global background concentrations (Simpson et al., 2012). Each air sample is collected for 1 min in a canister when the wind is blowing from the ocean. Air samples are collected over a three-week period covering every season in a single year. We follow the method used by Simpson et al. (2012) and average the data into 16 latitudinal bands, which have an equal volume of air for latitudinal average comparisons, weighting each band similarly. Data are available from 1985 to 2012, and we only use data that overlap the period of model simulations (2008 onward). The model monthly mean surface data are interpolated both spatially and temporally to the observational data before averaging into the same latitudinal bands as the observations. This ensures the model is only sampled where observational data exists. These latitudinal average concentrations are further averaged into four larger latitudinal bands shown in Figure 1. The number of observations averaged in each band and season are shown in Table S4.

3. Results

3.1. Global and Regional 2008 Baseline Emissions

A recent multimodel intercomparison project, POLMIP, showed that global models underestimated C_2H_6 when compared to surface and aircraft data, with particularly large biases in NH winter and spring (Emmons et al., 2015). As C_2H_6 is not formed in the atmosphere, this means that either the model OH is too high, resulting in too much loss from the atmosphere, or that the total emissions input into the models are too low. Even though the POLMIP multimodel global mean OH concentration was lower than other multimodel studies, it was still ~10% higher than OH estimates based on methyl chloroform observations (Monks et al., 2015). This means that model OH biases may play some role in simulating low C_2H_6. However, it is unlikely to explain all of the large model biases that were found by Emmons et al. (2015), with some of the bias likely to be a result of underestimated emissions. Negative biases in C_2H_6 have also been noted in other modeling studies using different global emission inventories and different models, suggesting that this is a widespread problem (Monks et al., 2017; Tilmes et al., 2016). Here we use our inverse modeling estimates of C_2H_6 to quantify the required global and regional scaling that should be applied to the baseline emissions in order to remove any model bias. We use 2008 as the baseline year as this is when observed NH C_2H_6 concentrations were at a minimum before they began to rise again in 2009 (Franco et al., 2016; Helmig et al., 2016). As we use off-line OH constrained by methyl chloroform observations, the inverse modeling results represent the change needed in emissions alone, removing the effect of any bias in TOMCAT-simulated OH.

Global and regional annual emissions from the a priori inventory, EMIS_PRIOR, and the inverse modeling estimates, EMIS_ANTH and EMIS_ALL, are shown in Figure 2 and Table S5. INVICAT increases EMIS_PRIOR from 7.3 to 14.9 Tg/year in EMIS_ANTH and to 15.4 Tg/year in EMIS_ALL, with monthly grid cell error reduction reaching up to 85% in North American and East Asian regions. This is approximately a factor of 2 increase in both inversions and are larger than emissions taken from some widely available global inventories (POLMIP, HTAP v2, and MACCity), which have global annual emissions of 7.7–10.2 Tg/year (see Table S6) and have resulted in model simulations that underestimated atmospheric concentrations of C_2H_6 (Emmons et al., 2015; Franco et al., 2016; Tilmes et al., 2016).

EMIS_ANTH and EMIS_ALL are slightly larger than the emission estimate of 13.5 Tg/year calculated by Xiao et al. (2004; see Table S6). This estimate was derived by applying MERs to a 1998 anthropogenic CH_4 emission data set that had been optimized to minimize biases between a forward model simulation and surface observations of CH_4 (Xiao et al., 2004). Xiao et al. (2004) found good agreement with aircraft measurements over the Pacific, but this data set needed to be adjusted over Europe and Asia in order to match other observations which decreased the global emission total to 13 Tg/year (Xiao et al., 2008). A similar estimate of 13.2 Tg/year was calculated by Franco et al. (2016), who also used MERs to convert inverse estimates of North American anthropogenic CH_4 emissions to C_2H_6. However, when using the new C_2H_6 emissions, they found positive

biases in simulated summertime C_2H_6 over North America and Europe. This suggests that the emissions were not fully optimized, since biases in emissions from regions outside the United States were not adjusted. As Xiao et al. (2004) and Franco et al. (2016) used CH_4 to derive C_2H_6 emissions, uncertainties are introduced due to the large amount of regional variability in MERs and possible errors in correctly identifying different CH_4 sources (Franco et al., 2016; Helmig et al., 2016). The posterior emission estimates avoid these uncertainties by directly optimizing C_2H_6 emissions based on C_2H_6 observations. It should be noted that the years for which emission totals were derived by Xiao et al. (2004, 2008) and Franco et al. (2016) are not the same as those considered in this study, and so there are dangers inherent in making direct comparisons between the estimates. However, since these are some of the only recent studies that have attempted to quantify global ethane emissions, the similarity between the results is encouraging.

We calculate regional annual 2008 baseline emissions for EMIS_PRIOR, EMIS_ANTH, and EMIS_ALL, aggregated onto the land regions previously used in the TransCom inversion study (Gurney et al., 2002), shown in Figure 1a. Both EMIS_ANTH and EMIS_ALL suggest that the largest biases in EMIS_PRIOR occur in temperate Eurasia (TemEuras) and temperate North America (TemNA; Figure 2 and Table S5). In EMIS_ANTH, TemEuras, TemNA, and North Africa (NAfr) account for 37, 26, and 23% of the total global emission increase, respectively, and most of the error reduction in EMIS_ANTH occurs in the first two regions. When considering the anthropogenic-only component of EMIS_PRIOR and EMIS_ANTH (Figure 2b), which are derived by subtracting the prior biomass burning, oceanic and biogenic emissions from both, the posterior global anthropogenic emissions of C_2H_6 are ~12 Tg/year in 2008, making up 80% of the global emissions. This highlights the importance of this sector as a source of C_2H_6 in the atmosphere.

In EMIS_ALL, the relative contributions of TemEuras, TemNA, and NAfr to the total global change in emissions are slightly smaller (35, 23, and 18%, respectively) but still dominate the global change showing consistency between the two inversions. The slightly smaller contribution to the global emission change is because of the ability of the inversion to modify natural and biomass burning sources as well as anthropogenic sources in EMIS_ALL, which results in slightly larger contributions to the global change in emissions coming from TroSA, SAfr, and TroAs, where natural and biomass burning emissions contribute more to the atmospheric signal. As a result, the error reduction in the inversion in these regions is higher than in EMIS_ANTH, suggesting natural emissions biases exist in the inventories.

3.2. Evaluation of 2008–2012 Emission Estimates

Figure 3 shows observed profiles of C_2H_6 collected aboard the DC-8 aircraft during the ARCTAS-A and ARCTAS-C/B campaigns over North America and parts of the Arctic during April and June–July 2008. Model-simulated monthly mean 2008 C_2H_6 has been interpolated both horizontally and vertically to the aircraft position, and both simulated and observed C_2H_6 has been averaged into 50-hPa altitude bins. In RUN_PRIOR, the model simulates low C_2H_6 abundances throughout the troposphere, with a mean bias error (MBE; see section S1) of −943 ppt (mean bias percent error (MBPE; see section S1) = −50%) in April and a smaller MBE of −361 ppt (−37%) in June–July. This is in line with previous studies (e.g., Emmons et al., 2015). The simulations which use the newly generated INVICAT posterior emissions result in MBEs of 98 and 115 ppt (21 and 24%) in April and −82 and −7 ppt (3 and 1%) in June–July in RUN_ANTH and RUN_ALL, respectively, and are consistently within the error bars of the observations. This shows that the new a posteriori emissions result in a much better simulation of tropospheric C_2H_6 abundances over North America in 2008, with only small differences between the MBPEs when using the two different inverse estimates.

Figure 4 shows seasonal mean surface C_2H_6 mixing ratios measured from flasks collected in remote regions throughout the Pacific between 2008 and 2012 which can be used to evaluate the emission inventories over several latitudes and years. The data have been averaged into four latitudinal bands, 48.6–90°N, 14.5–48.6°N, 14.5°S–14.5°N, and 48.6–14.5°S. The observations show average annual mean mole fractions over 2008–2013 that peak at 1431 ppt in the high northern latitudes. C_2H_6 then decreases from north to south to 1045 ppt in the NH midlatitudes (Figure 4b), 400 ppt in the tropics (Figure 4c), and 215 ppt in the SH midlatitudes (Figure 4d). The observations show a pronounced seasonal cycle outside of the tropics, with spring maxima and autumn minima.

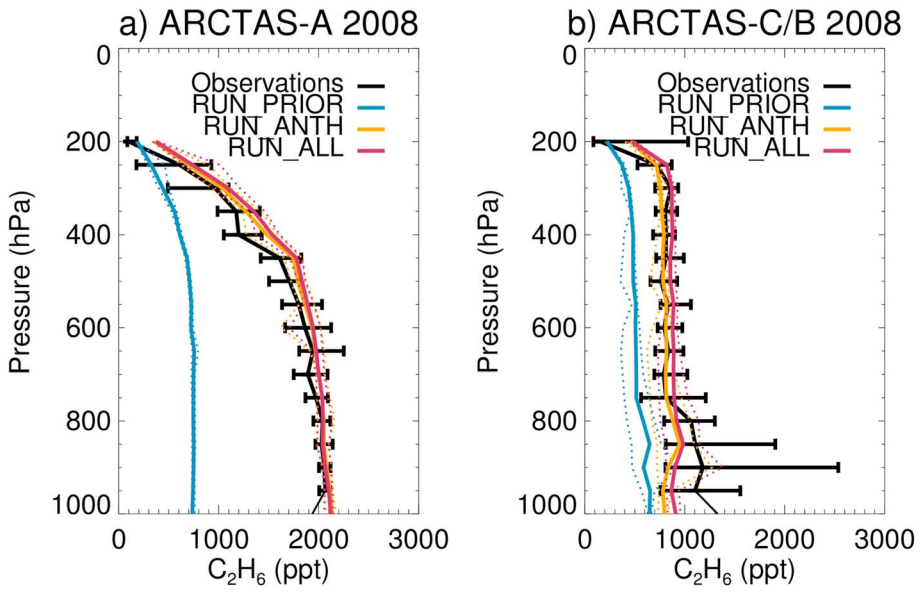

Figure 3. Model-observation comparisons of profiles of C_2H_6 (ppt) for the 2008 ARCTAS DC-8 aircraft campaigns during (a) April 2008 (ARCTAS-A) and (b) June–July 2008 (ARCTAS-CARB and ARCTAS-B). The solid lines show the median mole fractions in each bin, and the dashed lines and error bars show the 25th and 75th percentiles for the model and observations, respectively.

In RUN_PRIOR, TOMCAT simulates low C_2H_6 abundances in all four latitude bands, further supporting the assumption that the prior global emissions of C_2H_6 are underestimated. This simulation has a MBE (MPBE) of −830 ppt (−54%) in the 48.6–90°N band, −499 ppt (−44%) in the 14.5–48.6°N band, −113 ppt (−26%) in the 14.5°S–14.5°N band, and −44 ppt (−16%) in the 48.6–14.5°S band. TOMCAT does simulate a N-S gradient in C_2H_6; however, due to a larger model bias in the NH, the gradient is smaller than observed. It is worth noting that the largest model bias is found in the region where the majority of anthropogenic emissions occur. The model captures the timing of the seasonal C_2H_6 maxima and minima. However, the simulated amplitude of the seasonal cycle is smaller than observed, with the largest model biases occurring during the spring maxima. Simpson et al. (2012) compared the flask data to observations collected at several continuous monitoring sites and concluded that these observations are mostly representative of global background concentrations, suggesting that RUN_PRIOR has a negative bias throughout the whole troposphere, persisting throughout the year in the NH and half of the year in the SH.

When the larger a posteriori emissions are used in TOMCAT, the model simulates higher C_2H_6 globally (Figure 4). RUN_ANTH and RUN_ALL have MBEs of −2 and −7 ppt (1 and 1%) in the 48.6–90°N region, 81 and 81 ppt (11 and 11%) in the 14.5–48.6°N region, 118 and 158 ppt (32 and 42%) in the 14.5°S–14.5°N region, and 26 and 9 ppt (14 and 5%) in the 48.6–14.5°S region. These simulations show much better agreement with the observations than RUN_PRIOR in all regions except the tropics, where the model bias switches from negative to positive. Considering the MBPEs, the best model-observation agreement is now found in the high NH latitudes, which is where RUN_PRIOR has the largest bias. The model also simulates a more realistic seasonal cycle with a larger amplitude in the latitude bands outside of the tropics. In the tropics, difficulties in capturing tropical dynamics, such as the location of the Intertropical Convergence Zone or tropical convection, or insufficient assimilated observational data may be contributing to inaccuracies in the posterior model emission estimates, resulting in no improvement in the simulations in this region when compared to UCI data. However, it is worth noting that the inversions result in RUN_ANTH and RUN_ALL matching the tropical assimilated surface data well, including at Ascension Island when particularly high abundances are observed between 2011 and 2014 (Figure S1). Data at the Brazilian site ABP are not available after 2010, so South American emissions will be mostly controlled by high concentrations at Ascension Island from that point onward.

As found with the aircraft data comparison and when compared to FTIR data (Figure S2), the two posterior emission data sets are very similar and result in differences in the MPBE of a few percent in the NH.

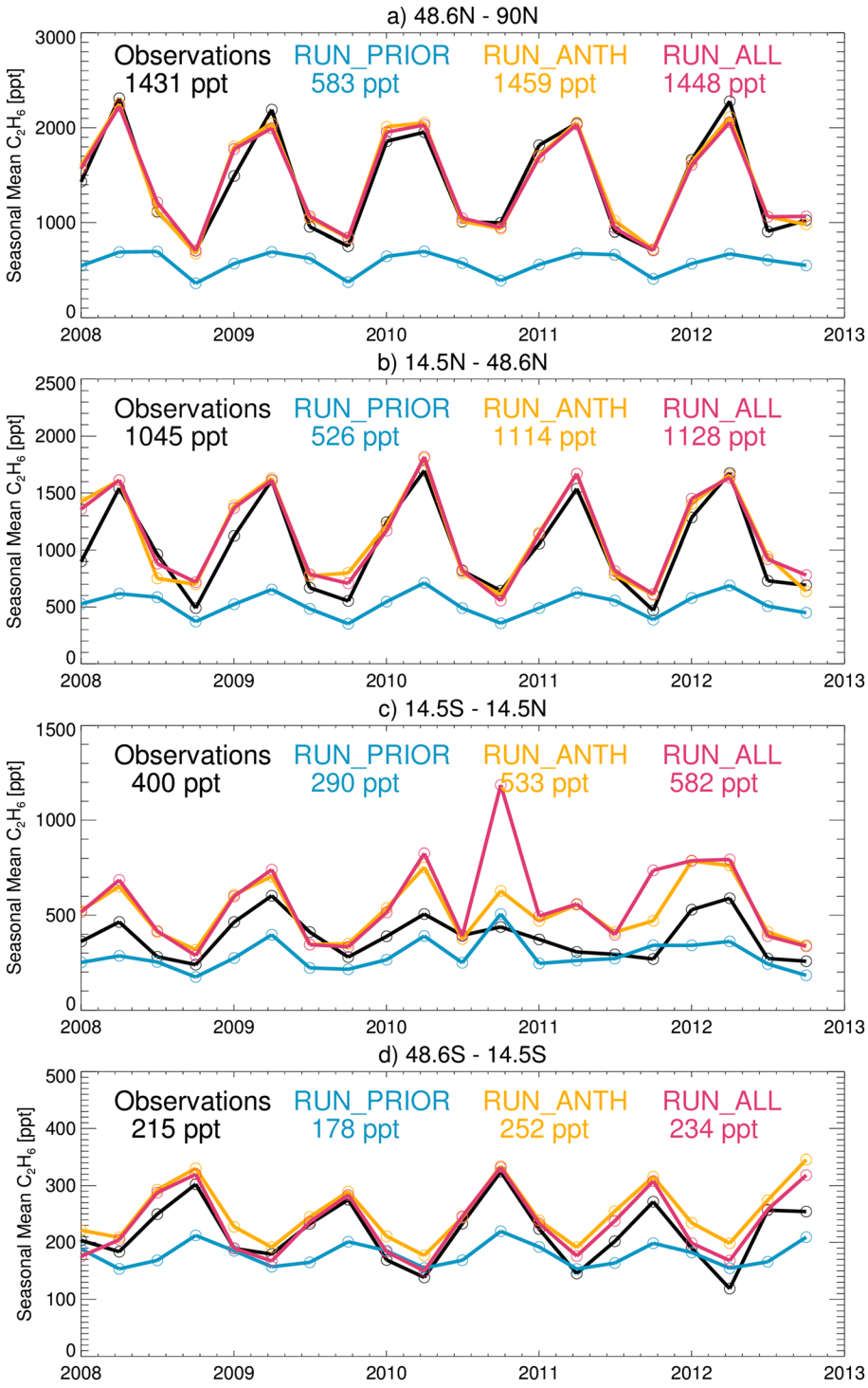

Figure 4. Observed and simulated seasonal mean C_2H_6 (ppt) averaged over four regions: (a) 48.6°N–90°N, (b) 14.5°N–48.6°N, (c) 14.5S–14.5°N, and (d) 48.6°S–14.5°S. The regional annual mean mole fractions averaged over 2008–2012 are noted on each panel.

However, in the SH, RUN_ALL has a lower MPBE than RUN_ANTH (5 compared to 14%) due to better agreement during the austral summer/autumn. This shows that when INVICAT is allowed to adjust emissions from other nonanthropogenic sources, the extra degrees of freedom can result in a better overall simulation. This is further evidence that prior estimates of natural and biomass burning emissions

are also uncertain and require more evaluation in regions where they make up a bigger fraction of the total emission.

3.3. Effects of Baseline Emission Changes on Tropospheric Chemistry

The simulations FC_RUN_PRIOR and FC_RUN_ALL use the full chemistry scheme and therefore demonstrate the effects of changing the baseline 2008 C_2H_6 emissions on other reactive gases such as O_3, PAN, and CH_3CHO (see Figure 5 and Figure S3). Larger C_2H_6 emissions in FC_RUN_ALL cause higher simulated mixing ratios of CH_3CHO due to increased oxidation of C_2H_6. The largest changes in terms of absolute mixing ratios are found near C_2H_6 emissions, with up to 36 ppt more CH_3CHO at the surface (Figure 5f) and up to 7 ppt at 500 hPa (Figure 5n). The largest increase in the burden of CH_3CHO occurs during winter and spring in the mid to high NH latitudes (Figure S3). Comparisons to aircraft data have shown that models underestimate CH_3CHO by ~10–100% in the NH (Emmons et al., 2015). The additional production of CH_3CHO from the increased C_2H_6 emissions will likely reduce these model biases.

The larger C_2H_6 emissions also lead to an increase in annual mean PAN mixing ratios of up to 38 ppt at the surface (Figure 5g) and 21 ppt at 500 hPa (Figure 5o). This is due to CH_3CHO being a source of PAN in the presence of NO_x (Fischer et al., 2014). Aircraft data have shown a range of model performances with respect to PAN, with some models underestimating PAN by up to 90% and some models overestimating PAN by up to 130% in the NH (Emmons et al., 2015). This suggests that correcting C_2H_6 emissions could cause a larger bias in PAN simulations in some models, while reducing the model bias in others.

Simulated O_3 is higher in FC_RUN_ALL due to the larger C_2H_6 emissions, with a maximum annual mean change of 0.4 ppb at the surface (Figure 5h) and 0.2 ppb at 500 hPa (Figure 5p). Most of the change at the surface occurs over the oceans. This is likely a result of additional PAN production in the model from C_2H_6 contributing to the transport of NO_x to remote regions. The lower reactivity of C_2H_6 compared to other NMHCs (Carter, 1994; Jenkin & Clemitshaw, 2000) tends to result in a lower O_3 production efficiency. This is most likely why increasing the global C_2H_6 emissions has a relatively small effect on annual mean O_3. The largest impact on O_3 is during summer when photochemical production is more efficient (Figure S3) and monthly mean surface O_3 increases by up to 0.8 ppb in August (Figure S4).

3.4. Trends in C_2H_6 Emissions Between 2008 and 2014

Least squares linear regression has been used to estimate the trends between 2008 and 2014 in the three emission data sets. EMIS_PRIOR has a very small and uncertain negative trend in global C_2H_6 emissions (-0.04 ± 0.61 Tg/yr^2; Figure 6a and Table 2). However, EMIS_ANTH and EMIS_ALL show positive trends in C_2H_6 emissions of 0.30 ± 0.28 and 0.33 ± 0.44 Tg/yr^2, respectively. These global trends are not significant over the time period studied ($p > 0.01$). Positive trends in C_2H_6 emissions of 0.42 ± 0.19 and 0.13–1.36 Tg/yr^2 were also estimated by Helmig et al. (2016) for 2009.5–2014.5 and Hausmann et al. (2016) for 2007–2014, respectively. Our estimates are within but toward the lower end of these ranges. Differences in the estimates are likely driven by differences in the approach used to calculate the trend and slightly different time periods considered. Helmig et al. (2016) applied the 4.2%/year trend in C_2H_6 concentrations observed at Jungfraujoch, Switzerland, to a global emission inventory for 2009. Hausmann et al. (2016) used a two-box model and observations from Zugspitze, Germany, and Lauder, New Zealand, to estimate trends in the emissions. Our estimates incorporate observations from many more locations, and accounts for interannual variations in atmospheric transport, giving a more detailed representation of regional emission trends.

The only statistically significant positive regional trend is in the TemNA region (see Figure 6b and Table 2), where EMIS_ANTH and EMIS_ALL have trends of 0.20 ± 0.11 and 0.24 ± 0.13 Tg/yr^2 ($p \leq 0.01$). This supports the proposals of previous studies that increased U.S. O&NG production are likely to contribute to the observed increases in C_2H_6 over North America and Europe from 2009 to 2015 (Franco et al., 2016; Helmig et al., 2016). Our estimate is slightly larger in magnitude than the emission trend estimated by Franco et al. (2016) who, in order to match concentrations observed at FTIR monitoring sites in North America, increased North American C_2H_6 emissions in a global model by 0.17 Tg/yr^2 between 2008 and 2014. It is worth noting that when 2008 is excluded from our analysis, the 2009–2014 trend in TemNA is even larger (0.29 ± 0.14 Tg/yr^2 in EMIS_ANTH and 0.32 ± 0.16 Tg/yr^2 in EMIS_ALL).

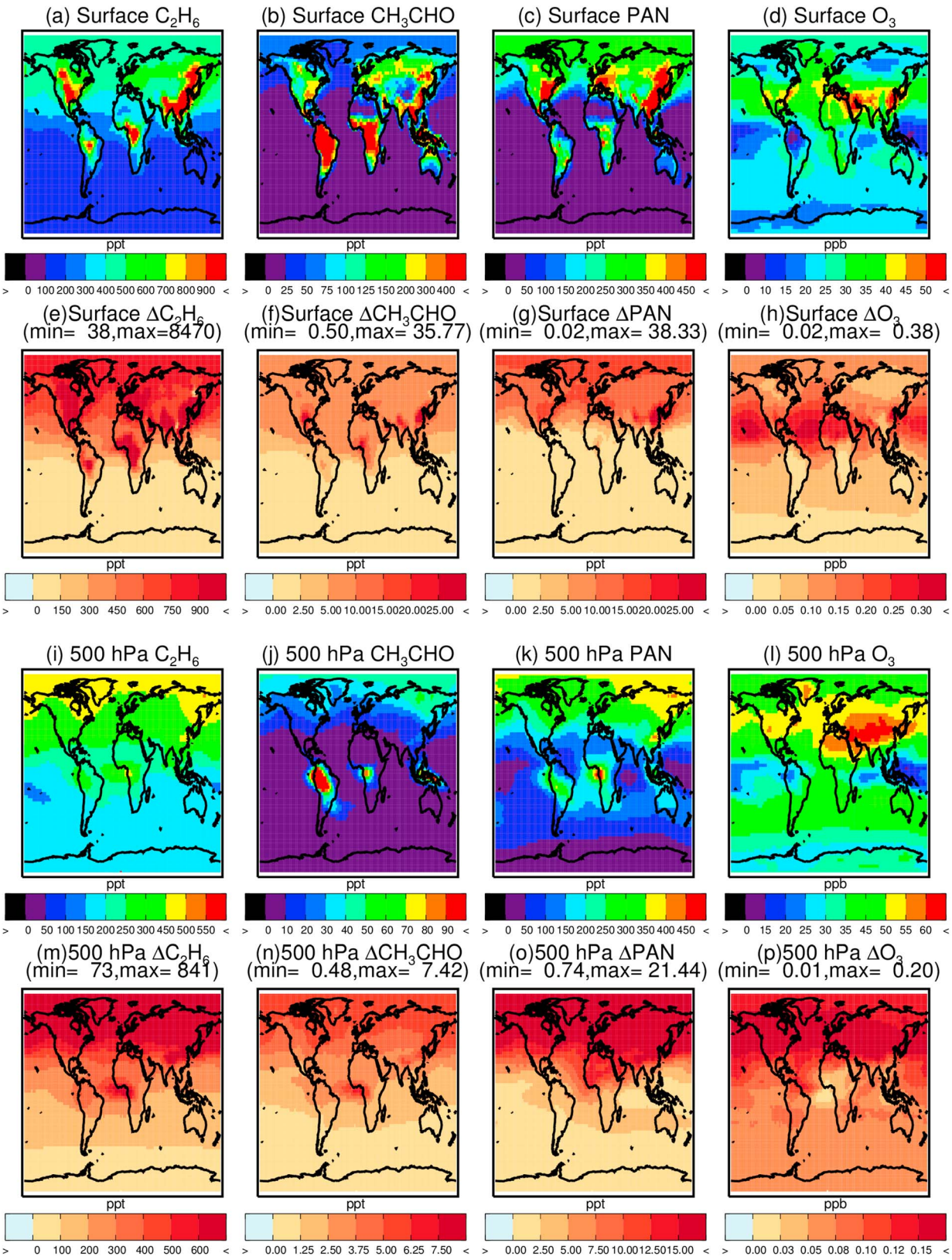

Figure 5. Simulated annual mean abundances of C_2H_6, O_3, PAN, and CH_3CHO at the surface (a–d) and at 500 hPa (i–l) from FC_RUN_PRIOR, alongside the mole fraction change when emissions are changed from EMIS_PRIOR to EMIS_ALL in FC_RUN_ALL at the surface (e–h) and at 500 hPa (m–p). The minimum and maximum values are given in each panel's subtitle.

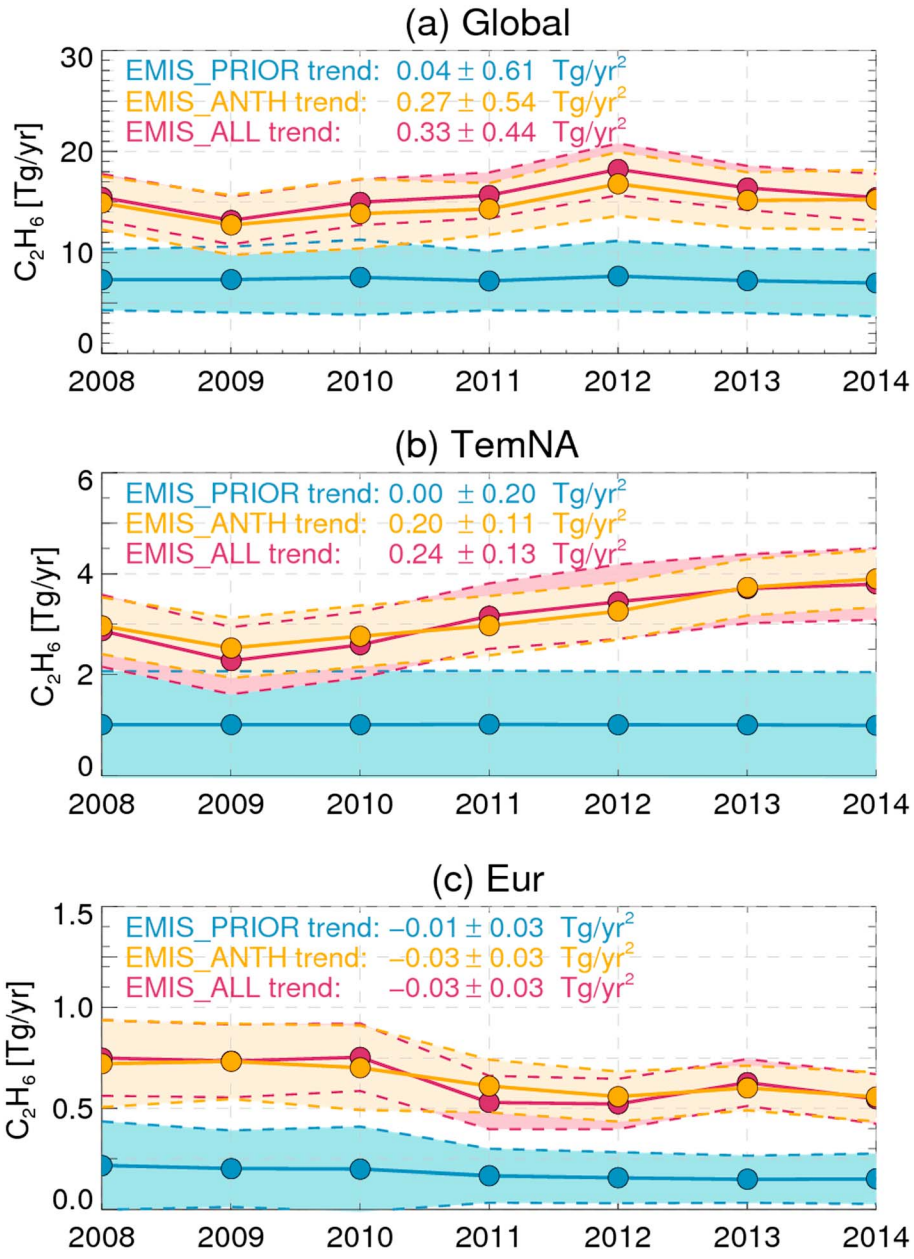

Figure 6. Annual C_2H_6 emissions (Tg/year) from the a priori inventory (EMIS_PRIOR) compared to the a posteriori emissions estimated by INVICAT (EMIS_ANTH and EMIS_ALL).

Not that all regions show an increase in emissions over this period (Figure S5). A negative trend of -0.01 ± 0.03 Tg/yr^2 is found in EMIS_PRIOR over Europe (Figure 6c and Table 2). Our inversion results suggest that European emissions have a larger significant negative trend of -0.03 ± 0.03 Tg/yr^2 ($p < 0.05$) in EMIS_ANTH due to underestimated baseline emission in EMIS_PRIOR. A significant trend of -0.18 ± 0.19 Tg/yr^2 is also found in TroAS in EMIS_ALL. However, both these regions have uncertainties as large as the trend.

The similarity of the trends in the NH between EMIS_ANTH and EMIS_ALL suggests that these trends are anthropogenic in nature. However, differences in tropical regions, such as TroAs, suggest that there may be some role played by nonanthropogenic emissions in the tropics, although these regions are not so well constrained by the inversion.

Table 2
Regional Trends in Emissions of C_2H_6 Between 2008 and 2014 From EMIS_PRIOR, EMIS_ANTH, and EMIS_ALL (Tg $[C_2H_6]/yr^2$)

Region	Trend in EMIS_PRIOR (Tg/yr^2)	Trend in EMIS_ANTH (Tg/yr^2)	Trend in EMIS_ALL (Tg/yr^2)	Ratio of EMIS_ANTH 2014 emissions to 2008 emissions	Ratio of EMIS_ALL 2014 emissions to 2008 emissions
Global	0.04 ± 0.61	0.30 ± 0.54	0.33 ± 0.44	1.02	1.00
TemEuras	0.00 ± 0.32	−0.05 ± 0.25	0.01 ± 0.23	1.00	1.00
TemNA	0.00 ± 0.20	0.20 ± 0.11*	0.24 ± 0.13*	1.31	1.32
TroAs	0.00 ± 0.31	−0.05 ± 0.30	−0.18 ± 0.19*	0.67	0.34
NAfr	0.00 ± 0.15	0.19 ± 0.15	0.20 ± 0.13	1.09	1.21
Oceans	0.00 ± 0.04	0.00 ± 0.04	0.00 ± 0.04	1.01	1.03
SAfr	0.00 ± 0.14	0.08 ± 0.14	0.13 ± 0.12	1.04	0.77
TroSA	−0.04 ± 0.13	−0.04 ± 0.13	−0.08 ± 0.10	0.60	0.65
Eur	−0.01 ± 0.03*	−0.03 ± 0.03	−0.03 ± 0.03	0.77	0.73
BorEuras	0.01 ± 0.09	0.02 ± 0.09	0.05 ± 0.05	0.98	2.82
TemSA	−0.01 ± 0.04	−0.02 ± 0.04	−0.02 ± 0.03	0.52	0.60
BorNA	0.01 ± 0.04*	0.01 ± 0.04	0.01 ± 0.02	1.65	1.85
Aus	0.00 ± 0.01	0.00 ± 0.01	0.00 ± 0.01	1.04	0.85

Note. Numbers followed by asterisks are significant at the 99% CL ($p \leq 0.01$).

3.5. Trends in C_2H_6 Atmospheric Abundances Between 2009 and 2014

RUN_PRIOR, RUN_ANTH, and RUN_ALL can be used to examine the regional changes in C_2H_6 concentrations when emissions are corrected in the simplified chemistry model, taking account of atmospheric transportation effects. Figure 7 shows the simulated trends (estimated by linear regression) in C_2H_6 from the three simulations at the surface and 700 hPa. RUN_PRIOR shows a small negative trend in background C_2H_6 in the NH and the tropics (−10 to 0 ppt/year) and a small positive trend in background C_2H_6 in the SH (0 to 10 ppt/year; Figures 7a and 7b). When using the corrected emissions in RUN_ANTH and RUN_ALL, the trend in background C_2H_6 in the NH and tropics switch from a negative trend to a positive trend (0 to 10 ppt/year), with some regions showing trends up to 50 ppt/year in continental outflow from the United States. This switch in the background C_2H_6 trend is driven by changes in emissions in the United States, Asia, and Africa (see section 3.4), where C_2H_6 generally shows positive trends of 10–600 ppt/year at the surface, with some locations having trends greater than 600 ppt/year. In the United States, the largest trends (~1,000 ppt/year) are found in the central regions, co-located with the largest positive trends in emissions (Figure S5). However, it is worth noting that this particularly large trend is in one grid box which is being affected by local O&G emissions and is not significant due to large interannual variability.

At 700 hPa, where air has undergone more mixing with background C_2H_6, smaller trends of up to 200 ppt/year are found over the United States and Asia in RUN_ANTH and RUN_ALL. At this altitude, the large-scale transportation patterns that C_2H_6 emissions undergo are visible, with emissions from the United States being transported in a north-east direction over the Atlantic toward Europe. This indicates that changes in the U.S. emissions are contributing to increased C_2H_6 concentrations downwind over Europe. Franco et al. (2015) reported a positive trend of 4.35×10^{14} molecules cm^2 yr in total column C_2H_6 FTIR measurements between 2009 and 2014 at Jungfraujoch, Switzerland. The simulated trend in TOMCAT total column C_2H_6 at this location (without averaging kernels applied) is -0.40×10^{14} molecules cm^2 yr in RUN_PRIOR. When TOMCAT is run using the posterior emissions, a positive trend of 2.63×10^{14} molecules cm^2 yr and 2.40×10^{14} molecules cm^2 yr is simulated in RUN_ANTH and RUN_ALL, respectively. While this is a more accurate representation of trends than those simulated in RUN_PRIOR, the model is still underestimating the trend by a factor of ~2. Reasons for these differences may be due to model errors when simulating long-range transport and boundary layer venting. It may also be due to a lack of observational data to constrain emissions in some regions, and future inverse model simulations may be improved through the assimilation of FTIR observations in regions where surface observations are lacking, such as Europe and Asia.

Over eastern Europe and tropical Asia, we see the effects of the negative trend in the posterior Eur and TroAs emissions as discussed in section 3.4. These emissions result in C_2H_6 trends of between −10 and −400 ppt/year at the surface in RUN_ANTH and RUN_ALL, with the largest trends seen in TroAs in line

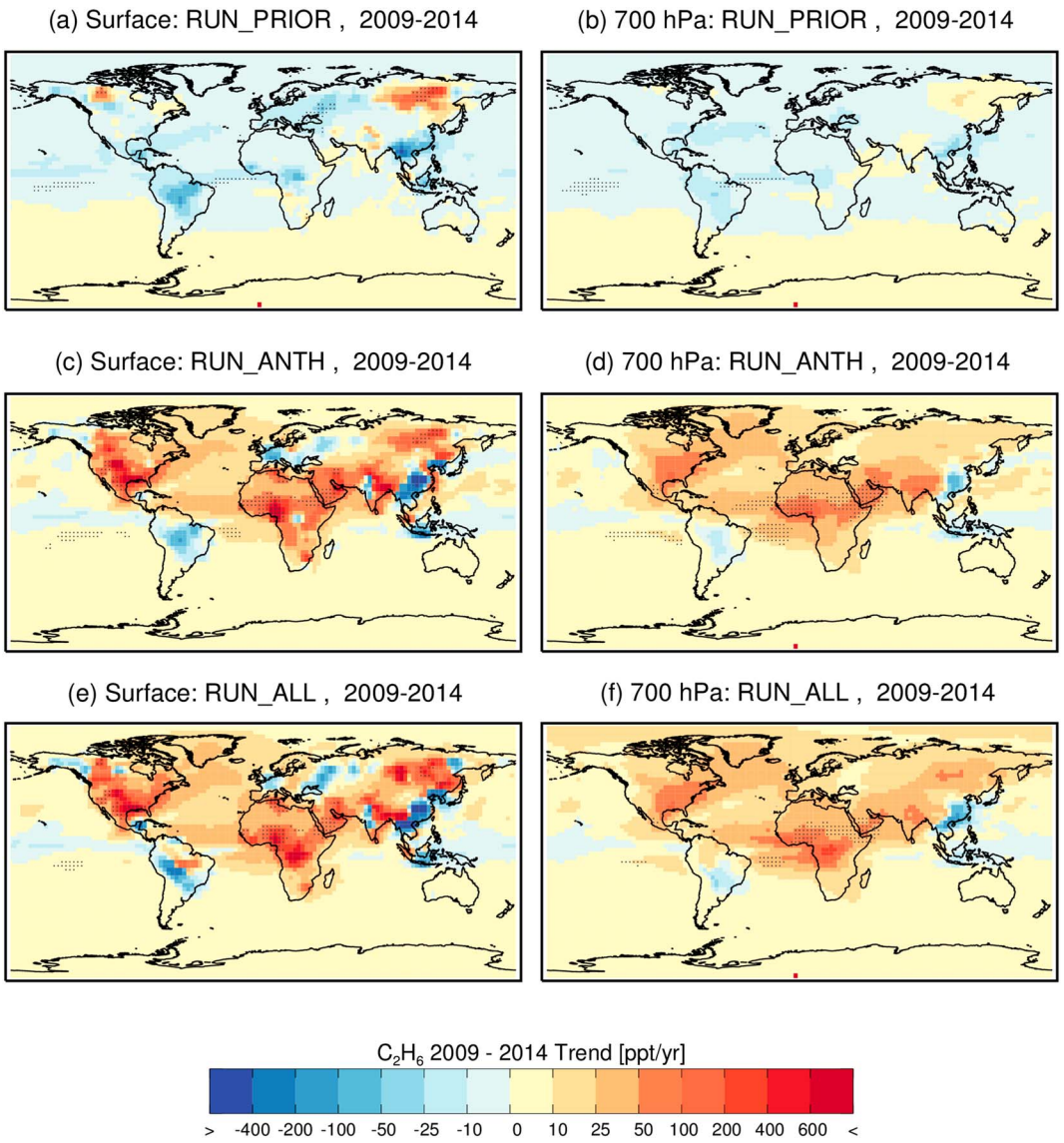

Figure 7. Simulated trends in C_2H_6 between 2009 and 2014 (ppt/year) from RUN_PRIOR (a and b), RUN_ANTH (c and d), and RUN_ALL (e and f) at the surface (a, c, and e) and at 700 hPa (b, d, and f). Trends that are significant at the 95% confidence level ($p < 0.05$) are indicated by the black dots.

with the largest significant negative emission trend. As expected from the similarity in the emissions between EMIS_ANTH and EMIS_ALL, RUN_ANTH and RUN_ALL show very similar regional patterns in C_2H_6.

3.6. Implications for Other NMHCs and CH_4

O&NG fugitive emissions are known to contain CH_4 and other NMHCs in addition to C_2H_6 (Brandt et al., 2014; Gilman et al., 2013; Howarth et al., 2011; Swarthout et al., 2013). Therefore, our results suggest that emissions of CH_4 and other NMHCs may have also increased between 2009 and 2014 in conjunction with C_2H_6. Depending on the size of these emissions, they have the potential to offset climate and air quality benefits that are expected from decreasing emissions of CO_2 and NO_x due to the reduction in the use of coal (de Gouw et al., 2014).

The need to understand the magnitude of fugitive emissions during a time of increasing O&NG production in the United States has driven a number of observation-based estimates of fossil fuel emissions of CH_4 (e.g., Karion et al., 2015; Peischl et al., 2016; Yuan et al., 2015) and NMHCs (Gilman et al., 2013; Pétron et al.,

2014; Warneke et al., 2014). Due to the co-emission of C_2H_6 with other species, their concentrations are often correlated downwind of regions where O&NG emissions occur (e.g., Hausmann et al., 2016; Yacovitch et al., 2014). These relationships are often used to calculate emission ratios of one chemical compound to another. CH_4 has received the most attention due to its high global warming potential, and for this reason, methane-to-ethane emission ratios (MERs) are most commonly reported (e.g., Helmig et al., 2016; Kang et al., 2014; Smith et al., 2015; Peischl et al., 2015). Table S7 shows several mass MERs calculated from observations made near O&NG production facilities reported in different studies. Using the median MER (10.9) and the 0.20 ± 0.10-Tg/yr^2 C_2H_6 emission trend calculated from EMIS_ANTH, our results suggest that CH_4 emissions in the United States could have increased simultaneously at a rate of 2.18 ± 1.09 Tg/yr^2 between 2008 and 2014.

After almost a decade of very little growth, atmospheric CH_4 has increased since 2007 (Frankenberg et al., 2011; Nisbet et al., 2014; Rigby et al., 2008; Sussmann et al., 2012). The source of the recent increase is still not fully understood, but may be due to increases in emissions (Rigby et al., 2008) or changes to the chemical sink (Rigby et al., 2017; Turner et al., 2017). In addition, even if changes in emissions played a part in the recent increase in atmospheric CH_4 concentrations, debate still exists over whether natural or anthropogenic emissions are the dominant contributor (Bergamaschi et al., 2013; Hausmann et al., 2016; Kirschke et al., 2013; Schaefer et al., 2016). Turner et al. (2016) suggested that a trend in U.S. CH_4 emissions of 2.2 Tg/yr^2 could be derived by partitioning satellite measurements over the continent and measurements of background concentrations over the Pacific Ocean. However, Bruhwiler et al. (2017) showed that this trend was not necessarily robust, mainly due to the sparseness of the observations in time and the sensitivity of the derived trend to the location chosen to represent the background concentration of CH_4. They suggested that a much smaller trend in U.S. CH_4 emissions (or no trend at all) might be more consistent with the satellite observations. Worden et al. (2017) showed that it was possible to reconcile growing fossil fuel emissions of CH_4 with the concurrent decrease in heavy isotopes of the species, finding that increasing fossil fuel emissions of CH_4 could be responsible for 12–19 Tg/year of the global annual increase. Our estimate of 2.18 ± 1.09 Tg/yr^2 from the United States could certainly contribute to that figure. However, due to the large range of MERs that have been presented in observational studies (Table S7; MERs = 7.3–95.7) and the difficulty in upscaling these MERs to provide country-wide emission data, the uncertainty of our derived trend in US O&NG CH_4 emissions are relatively high and it is therefore difficult to say with confidence to what extent increased fossil fuel activity in the United States is contributing to the observed increase in the global atmospheric CH_4.

4. Conclusions

For the first time, we have performed a global inversion for emissions of C_2H_6 using a simplified chemistry scheme for C_2H_6, off-line global OH concentrations previously constrained by methyl chloroform, and the assimilation of flask observations of C_2H_6 with the purpose of fulfilling three main aims.

First, we used the inversions to improve the performance of a baseline emission inventory used in global models for the year 2008, removing significant biases which were displayed in previous studies (e.g., Emmons et al., 2015). Our results indicate that the prior emission data set that we used, which has a total global C_2H_6 emission of 7.3 ± 3.03 Tg/year, was approximately a factor of 2 too small. Our posterior inventories indicate that emissions were 14.9 ± 2.6 to 15.4 ± 2.3 Tg/year in 2008. We found that the largest increase in emissions between the prior and posterior inventories occurred in temperate North America (23–26%) and temperate Asia (35–37%). Comparisons with unassimilated observational flask data collected at the surface and on board an aircraft showed that the TOMCAT model was better able to capture the magnitude and seasonality of C_2H_6 as well as the NH-SH gradient. However, due to a relative lack of assimilated tropical observational data near South America and/or model transport errors, the comparison to independent flask observations in the tropics is not as good as elsewhere. This could be improved by extra monitoring stations.

Second, we evaluated the effect of the improved C_2H_6 emissions on other chemical species using the TOMCAT full chemistry model. The near doubling of the C_2H_6 emissions led to increases in CH_3CHO, PAN, and O_3. Several models have shown negative biases in CH_3CHO (Emmons et al., 2015) and improving C_2H_6 emissions may offer some improvements in the simulation of this species.

Third, we used our inverse model results to quantify the scale of global or regional trends in C_2H_6 emissions between 2008 and 2014, a period when atmospheric C_2H_6 increased at a number of NH surface sites. Our inversions produce trends in global C_2H_6 emissions of 0.30 ± 0.54 and 0.33 ± 0.44 Tg/yr^2. A statistically significant regional trend of 0.20 ± 0.11 and 0.24 ± 0.13 Tg/yr^2 is found in the posterior emissions in temperate North America, a region which covers the United States. This trend results in a 31–32% increase in 2014 emissions relative to 2008 emissions over North America. Our inversion results corroborate the theory that increased O&NG production in the United States has led to an increase in NH C_2H_6 atmospheric concentrations since 2009. If the previous estimate that the Bakken region is contributing an annual growth rate of 0.06 Tg/yr^2 to global emissions (Kort et al., 2016) is accurate, then this region alone could be contributing approximately 25–30% of the North American trend according to our results. Unfortunately, the grid resolution and posterior uncertainty in our inversions does not allow us to comment further on the subregional distribution of the emissions.

While our inversions are an improvement over previous studies, since they directly assimilate C_2H_6 observations rather than using MERs to estimate C_2H_6, our results are not without uncertainty. Future inversions could be improved by taking account of year-to-year changes in the magnitude of the atmospheric OH sink. Rigby et al. (2017) and Turner et al. (2017) have recently raised the possibility that there has been a negative trend in OH concentrations since 2009, which would lead to an increase in the atmospheric burden of C_2H_6. However, the level of uncertainty surrounding the size of the OH sink is still large (Rigby et al., 2017), and therefore, attempting to account for changes in OH is outside the scope of this study. Our results could also be made more robust with the assimilation of more C_2H_6 observations in regions where they are scarce, such as in the SH, tropics, and Eurasia. Our study highlights the importance of continued long-term global measurements which can be used for constraining global chemical models and their inventories and provides a better understanding of long-term changes in emissions.

Acknowledgments

C.W. was supported by the UK Natural Environment Research Council (NERC) through funding for the National Centre for Earth Observation (NCEO). The National Center for Atmospheric Research (NCAR) is funded by the National Science Foundation. Computing resources were provided by UK National Super Computing Service and the National Oceanic Atmospheric Administration. The VOC analyses from the Global Greenhouse Gas Reference Network are funded by U.S. National Oceanic and Atmospheric Administration's Climate Program Office's AC4 Program. Quality assurance is facilitated by overlapping flask in situ VOC monitoring at Summit, Greenland, funded by the National Science Foundation Arctic Observing Network, grant 1108391. UCI ARCTAS data were funded by the NASA Global Tropospheric Chemistry Program, the NASA Radiation Sciences Program, and the California Air Resources Board. Pacific UCI flask measurements (to 2012) were funded by NASA (grant NAG5-8935). The authors acknowledge Stu McKeen at NOAA/ESRL for providing the processed NEI 2011 emissions inventory (ftp://aftp.fsl.noaa.gov/divisions/taq/emissions_data_2011/), and Gabriele Pfister at NCAR for regridding these emissions. The FTIR observation program at Thule is supported by NASA. The posterior emissions created for this study are publicly available and can be downloaded from the Centre for Environmental Data Analysis (CEDA) Research Data Archive (doi:10.5285/9dace73ad8654298aea626b8bde0a782). Go to http://catalogue.ceda.ac.uk/uuid/9dace73ad8654298aea626b8bde0a782.

References

Alexe, M., Bergamaschi, P., Segers, A., Detmers, R., Butz, A., Hasekamp, O., et al. (2015). Inverse modelling of CH4 emissions for 2010–2011 using different satellite retrieval products from GOSAT and SCIAMACHY. *Atmospheric Chemistry and Physics*, *15*(1), 113–133. https://doi.org/10.5194/acp-15-113-2015

Babenhauserheide, A., Basu, S., Houweling, S., Peters, W., & Butz, A. (2015). Comparing the CarbonTracker and TM5-4DVar data assimilation systems for CO_2 surface flux inversions. *Atmospheric Chemistry and Physics*, *15*(17), 9747–9763. https://doi.org/10.5194/acp-15-9747-2015

Bell, M. L., McDermott, A., Zeger, S. L., Samet, J. M., & Dominici, F. (2004). Ozone and short-term mortality in 95 US urban communities, 1987–2000. *JAMA*, *292*(19), 2372–2378. https://doi.org/10.1001/jama.292.19.2372

Bergamaschi, P., Houweling, S., Segers, A., Krol, M., Frankenberg, C., Scheepmaker, R. A., et al. (2013). Atmospheric CH_4 in the first decade of the 21st century: Inverse modeling analysis using SCIAMACHY satellite retrievals and NOAA surface measurements. *Journal of Geophysical Research: Atmospheres*, *118*, 7350–7369. https://doi.org/10.1002/jgrd.50480

Bian, H., Colarco, P. R., Chin, M., Chen, G., Rodriguez, J. M., Liang, Q., et al. (2013). Source attributions of pollution to the western Arctic during the NASA ARCTAS field campaign. *Atmospheric Chemistry and Physics*, *13*(9), 4707–4721. https://doi.org/10.5194/acp-13-4707-2013

Blake, D. (2013). Methane, nonmethane hydrocarbons, alkyl nitrates, and chlorinated carbon compounds including 3 chlorofluorocarbons (CFC-11, CFC-12, and CFC-113) in whole-air samples. Carbon Dioxide Information Analysis Center, Oak Ridge National Laboratory, U.S. Department of Energy, Oak Ridge Tenn., U.S.A.

Blake, D. R., & Rowland, F. S. (1986). Global atmospheric concentrations and source strength of ethane. *Nature*, *321*(6067), 231–233. https://doi.org/10.1038/321231a0

Blake, N. J., Blake, D. R., Simpson, I. J., Meinardi, S., Swanson, A. L., Lopez, J. P., et al. (2003). NMHCs and halocarbons in Asian continental outflow during the transport and chemical evolution over the Pacific (TRACE-P) field campaign: Comparison with PEM-west B. *Journal of Geophysical Research*, *108*(D20), 8806. https://doi.org/10.1029/2002JD003367

Bousserez, N., Henze, D. K., Perkins, A., Bowman, K. W., Lee, M., Liu, J., et al. (2015). Improved analysis-error covariance matrix for high-dimensional variational inversions: Application to source estimation using a 3D atmospheric transport model. *Quarterly Journal of the Royal Meteorological Society*, *141*(690), 1906–1921. https://doi.org/10.1002/qj.2495

Brandt, A. R., Heath, G. A., Kort, E. A., O'Sullivan, F., Pétron, G., Jordaan, S. M., et al. (2014). Methane leaks from north American natural gas systems. *Science*, *343*(6172), 733–735. https://doi.org/10.1126/science.1247045

Bruhwiler, L. M., Basu, S., Bergamaschi, P., Bousquet, P., Dlugokencky, E., Houweling, S., et al. (2017). U.S. CH_4 emissions from oil and gas production: Have recent large increases been detected? *Journal of Geophysical Research: Atmospheres*, *122*, 4070–4083. https://doi.org/10.1002/2016JD026157

Brunekreef, B., & Holgate, S. T. (2002). Air pollution and health. *Lancet*, *360*(9341), 1233–1242. https://doi.org/10.1016/S0140-6736(02)11274-8

Carter, W. P. L. (1994). Development of ozone reactivity scales for volatile organic compounds. *Air & Waste*, *44*(7), 881–899. https://doi.org/10.1080/1073161X.1994.10467290

Chevallier, F., Bre'on, F.-M., & Rayner, P. J. (2007). Contribution of the orbiting carbon observatory to the estimation of CO_2 sources and sinks: Theoretical study in a variational data assimilation framework. *Journal of Geophysical Research*, *112*, D09307. https://doi.org/10.1029/2006JD007375

Chevallier, F., Fisher, M., Peylin, P., Serrar, S., Bousquet, P., Breon, F. M., et al. (2005). Inferring CO_2 sources and sinks from satellite observations: Method and application to TOVS data. *Journal of Geophysical Research*, *110*, D24309. https://doi.org/10.1029/2005JD006390

Chipperfield, M. P. (2006). New version of the TOMCAT/SLIMCAT off-line chemical transport model: Intercomparison of stratospheric tracer experiments. Quarterly journal of the royal. *Meteorological Society*, *132*(617), 1179–1203. https://doi.org/10.1256/qj.05.51

Collins, W. J., Derwent, R. G., Johnson, C. E., & Stevenson, D. S. (2002). The oxidation of organic compounds in the troposphere and their global warming potentials. *Climatic Change*, *52*(4), 453–479. https://doi.org/10.1023/A:1014221225434

Dalsøren, S. B., Myhre, G., Hodnebrog, Ø., Myhre, C. L., Stohl, A., Pisso, I., et al. (2018). Discrepancy between simulated and observed ethane and propane levels explained by underestimated fossil emissions. *Nature Geoscience*, *11*, 178–184.

de Gouw, J. A., Parrish, D. D., Frost, G. J., & Trainer, M. (2014). Reduced emissions of CO_2, NO_x, and SO_2 from U.S. power plants owing to switch from coal to natural gas with combined cycle technology. *Earth's Future*, *2*(2), 75–82. https://doi.org/10.1002/2013EF000196

Dee, D. P., Uppala, S. M., Simmons, A. J., Berrisford, P., Poli, P., Kobayashi, S., et al. (2011). The ERA-interim reanalysis: Configuration and performance of the data assimilation system. *Quarterly Journal of the Royal Meteorological Society*, *137*(656), 553–597. https://doi.org/10.1002/qj.828

Ehhalt, D. H., Dorn, H. P., & Poppe, D. (1990). The chemistry of the hydroxyl radical in the troposphere. Proceedings of the Royal Society of Edinburgh. Section B. *Biological sciences*, *97*, 17–34. https://doi.org/10.1017/S0269727000005273

Emmons, L. K., Arnold, S. R., Monks, S. A., Huijnen, V., Tilmes, S., Law, K. S., et al. (2015). The POLARCAT model Intercomparison project (POLMIP): Overview and evaluation with observations. *Atmospheric Chemistry and Physics*, *15*(12), 6721–6744. https://doi.org/10.5194/acp-15-6721-2015

Fischer, E. V., Jacob, D. J., Yantosca, R. M., Sulprizio, M. P., Millet, D. B., Mao, J., et al. (2014). Atmospheric peroxyacetyl nitrate (PAN): A global budget and source attribution. *Atmospheric Chemistry and Physics*, *14*(5), 2679–2698. https://doi.org/10.5194/acp-14-2679-2014

Franco, B., Bader, W., Toon, G. C., Bray, C., Perrin, A., Fischer, E. V., et al. (2015). Retrieval of ethane from ground-based FTIR solar spectra using improved spectroscopy: Recent burden increase above Jungfraujoch. *Journal of Quantitative Spectroscopy and Radiative Transfer*, *160*, 36–49. https://doi.org/10.1016/j.jqsrt.2015.03.017

Franco, B., Mahieu, E., Emmons, L. K., Tzompa-Sosa, Z. A., Fischer, E. V., Sudo, K., et al. (2016). Evaluating ethane and methane emissions associated with the development of oil and natural gas extraction in North America. *Environmental Research Letters*, *11*(4), 4. https://doi.org/10.1088/1748-9326/11/4/044010

Frankenberg, C., Aben, I., Bergamaschi, P., Dlugokencky, E. J., van Hees, R., Houweling, S., et al. (2011). Global column-averaged methane mixing ratios from 2003 to 2009 as derived from SCIAMACHY: Trends and variability. *Journal of Geophysical Research*, *116*, D04302. https://doi.org/10.1029/2010JD014849

Fraser, A., Palmer, P. I., Feng, L., Boesch, H., Cogan, A., Parker, R., et al. (2013). Estimating regional methane surface fluxes: The relative importance of surface and GOSAT mole fraction measurements. *Atmospheric Chemistry and Physics*, *13*(11), 5697–5713. https://doi.org/10.5194/acp-13-5697-2013

Gilman, J. B., Lerner, B. M., Kuster, W. C., & de Gouw, J. A. (2013). Source signature of volatile organic Compounds from oil and Natural gas operations in northeastern Colorado. *Environmental Science & Technology*, *47*(3), 1297–1305. https://doi.org/10.1021/es304119a

Granier, C., Bessagnet, B., Bond, T., D'Angiola, A., van der Gon, H. D., Frost, G. J., et al. (2011). Evolution of anthropogenic and biomass burning emissions of air pollutants at global and regional scales during the 1980–2010 period. *Climatic Change*, *109*(1-2), 163–190. https://doi.org/10.1007/s10584-011-0154-1

Granier, C., Lamarque, J., Mieville, A., Muller, J., Olivier, J., Orlando, J., et al. (2005). POET. http://www.aero.jussieu.fr/projet/ACCENT/POET.php

Guenther, A. B., Jiang, X., Heald, C. L., Sakulyanontvittaya, T., Duhl, T., Emmons, L. K., & Wang, X. (2012). The model of emissions of gases and aerosols from nature version 2.1 (MEGAN2.1): An extended and updated framework for modeling biogenic emissions. *Geoscientific Model Development*, *5*(6), 1471–1492. https://doi.org/10.5194/gmd-5-1471-2012

Gurney, K. R., Law, R. M., Denning, A. S., Rayner, P. J., Baker, D., Bousquet, P., et al. (2003). Transcom 3 CO_2 inversion Intercomparison: 1. Annual mean control results and sensitivity to transport and prior flux information. *Tellus B*, *55*(2), 555–579. https://doi.org/10.1034/j.1600-0889.2003.00049.x

Gurney, K. R., Law, R. M., Denning, A. S., Rayner, P. J., Baker, D., Bousquet, P., et al. (2002). Towards robust regional estimates of CO_2 sources and sinks using atmospheric transport models. *Nature*, *415*(6872), 626–630. https://doi.org/10.1038/415626a

Hakola, H., & Hellén, H. (2016). Atmospheric chemistry: The return of ethane. *Nature Geoscience*, *9*(7), 475–476. https://doi.org/10.1038/ngeo2736

Hausmann, P., Sussmann, R., & Smale, D. (2016). Contribution of oil and natural gas production to renewed increase in atmospheric methane (2007–2014): Top–down estimate from ethane and methane column observations. *Atmospheric Chemistry and Physics*, *16*(5), 3227–3244. https://doi.org/10.5194/acp-16-3227-2016

Helmig, D., Petrenko, V., Martinerie, P., Witrant, E., Röckmann, T., Zuiderweg, A., et al. (2014). Reconstruction of Northern Hemisphere 1950–2010 atmospheric non-methane hydrocarbons. *Atmospheric Chemistry and Physics*, *14*(3), 1463–1483. https://doi.org/10.5194/acpd-14-1463-2014

Helmig, D., Rossabi, S., Jacques, H., Tans, P., Montzka, S. A., Maserie, K., et al. (2016). Reversal of global atmospheric ethane and propane trends largely due to US oil and natural gas production. *Nature Geoscience*, *9*(7), 490–495. https://doi.org/10.1038/ngeo2721

Howarth, R. W., Santoro, R., & Ingraffea, A. (2011). Methane and the greenhouse-gas footprint of natural gas from shale formations. *Climatic Change*, *106*(4), 679–690. https://doi.org/10.1007/s10584-011-0061-5

Hudman, R. C., Jacob, D. J., Cooper, O. R., Evans, M. J., Heald, C. L., Park, R. J., et al. (2004). Ozone production in transpacific Asian pollution plumes and implications for ozone air quality in California. *Journal of Geophysical Research*, *109*, D23S10. https://doi.org/10.1029/2004jd004974

Huijnen, V., Williams, J., van Weele, M., van Noije, T., Krol, M., Dentener, F., et al. (2010). The global chemistry transport model TM5: Description and evaluation of the tropospheric chemistry version 3.0. *Geoscientific Model Development*, *3*(2), 445–473. https://doi.org/10.5194/gmd-3-445-2010

Jacob, D. J., Crawford, J. H., Maring, H., Clarke, A. D., Dibb, J. E., Emmons, L. K., et al. (2010). The Arctic research of the composition of the troposphere from aircraft and satellites (ARCTAS) mission: Design, execution, and first results. *Atmospheric Chemistry and Physics*, *10*(11), 5191–5212. https://doi.org/10.5194/acp-10-5191-2010

Jenkin, M. E., & Clemitshaw, K. C. (2000). Ozone and other secondary photochemical pollutants: Chemical processes governing their formation in the planetary boundary layer. *Atmospheric Environment*, *34*(16), 2499–2527. https://doi.org/10.1016/S1352-2310(99)00478-1

Kang, M., Kanno, C. M., Reid, M. C., Zhang, X., Mauzerall, D. L., Celia, M. A., et al. (2014). Direct measurements of methane emissions from abandoned oil and gas wells in Pennsylvania. *PNAS*, *111*(51), 18,173–18,177. https://doi.org/10.1073/pnas.1408315111

Karion, A., Sweeney, C., Kort, E. A., Shepson, P. B., Brewer, A., Cambaliza, M., et al. (2015). Aircraft-based estimate of total methane emissions from the Barnett shale region. *Environmental Science & Technology*, *49*(13), 8124–8131. https://doi.org/10.1021/acs.est.5b00217

Kirschke, S., Bousquet, P., Ciais, P., Saunois, M., Canadell, J. G., Dlugokencky, E. J., et al. (2013). Three decades of global methane sources and sinks. *Nature Geoscience*, *6*(10), 813–823. https://doi.org/10.1038/ngeo1955

Kort, E. A., Smith, M. L., Murray, L. T., Gvakharia, A., Brandt, A. R., Peischl, J., et al. (2016). Fugitive emissions from the Bakken shale illustrate role of shale production in global ethane shift. *Geophysical Research Letters*, *43*, 4617–4623. https://doi.org/10.1002/2016GL068703

Lamarque, J.-F., Bond, T. C., Eyring, V., Granier, C., Heil, A., Klimont, Z., et al. (2010). Historical (1850–2000) gridded anthropogenic and biomass burning emissions of reactive gases and aerosols: Methodology and application. *Atmospheric Chemistry and Physics*, *10*(15), 7017–7039. https://doi.org/10.5194/acp-10-7017-2010

McNorton, J., Chipperfield, M. P., Gloor, M., Wilson, C., Feng, W., Hayman, G. D., et al. (2016). Role of OH variability in the stalling of the global atmospheric CH_4 growth rate from 1999 to 2006. *Atmospheric Chemistry and Physics*, *16*(12), 7943–7956. https://doi.org/10.5194/acp-16-7943-2016

Meirink, J. F., Bergamaschi, P., Frankenberg, C., d'Amelio, M. T. S., Dlugokencky, E. J., Gatti, L., et al. (2008). Four-dimensional variational data assimilation for inverse modeling of atmospheric methane emissions: Analysis of SCIAMACHY observations. *Journal of Geophysical Research*, *113*, D17301. https://doi.org/10.1029/2007JD009740

Millet, D. B., Guenther, A., Siegel, D. A., Nelson, N. B., Singh, H. B., de Gouw, J. A., et al. (2010). Global atmospheric budget of acetaldehyde: 3-D model analysis and constraints from in-situ and satellite observations. *Atmospheric Chemistry and Physics*, *10*(7), 3405–3425. https://doi.org/10.5194/acp-10-3405-2010

Monks, S. A., Arnold, S. R., & Chipperfield, M. P. (2012). Evidence for El Niño-Southern Oscillation (ENSO) influence on Arctic CO interannual variability through biomass burning emissions. *Geophysical Research Letters*, *39*, L14804. https://doi.org/10.1029/2012GL052512

Monks, S. A., Arnold, S. R., Emmons, L. K., Law, K. S., Turquety, S., Duncan, B. N., et al. (2015). Multi-model study of chemical and physical controls on transport of anthropogenic and biomass burning pollution to the Arctic. *Atmospheric Chemistry and Physics*, *15*(6), 3575–3603. https://doi.org/10.5194/acp-15-3575-2015

Monks, S. A., Arnold, S. R., Hollaway, M. J., Pope, R. J., Wilson, C., Feng, W., et al. (2017). The TOMCAT global chemical transport model v1.6: Description of chemical mechanism and model evaluation. *Geoscientific Model Development*, *10*(8), 3025–3057. https://doi.org/10.5194/gmd-10-3025-2017

Montzka, S. A., Krol, M., Dlugokencky, E., Hall, B., Jöckel, P., & Lelieveld, J. (2011). Small interannual variability of global atmospheric hydroxyl. *Science*, *331*(6013), 67–69. https://doi.org/10.1126/science.1197640

Moss, R. H., Edmonds, J. A., Hibbard, K., Manning, M., Rose, S. K., van Vuuren, D. P., et al. (2010). The next generation of scenarios for climate change research and assessment. *Nature*, *463*(7282), 747–756. https://doi.org/10.1038/nature08823

Myhre, G., Shindell, D., Bréon, F.-M., Collins, W., Fuglestvedt, J., Huang, J., et al. (2013). Anthropogenic and natural radiative forcing. In T. F. Stocker, D. Qin, G.-K. Plattner, M. Tignor, S. K. Allen, J. Boschung, et al. (Eds.), *Climate Change 2013: The Physical Science Basis, Contribution of Working Group I to the Fifth Assessment Report of the Intergovernmental Panel on Climate Change* (chap. 8, 661 pp.). Cambridge, United Kingdom and New York, NY, USA: Cambridge University Press.

Nisbet, E. G., Dlugokencky, E. J., & Bousquet, P. (2014). Methane on the rise—Again. *Science*, *343*(6170), 493–495. https://doi.org/10.1126/science.1247828

Nocedal, J. (1980). Updating quasi-Newton matrices with limited storage. *Mathematics of Computation*, *35*(151), 773–782. https://doi.org/10.1090/S0025-5718-1980-0572855-7

Patra, P. K., Houweling, S., Krol, M., Bousquet, P., Belikov, D., Bergmann, D., et al. (2011). TransCom model simulations of CH_4 and related species: Linking transport, surface flux and chemical loss with CH_4 variability in the troposphere and lower stratosphere. *Atmospheric Chemistry and Physics*, *11*(24), 12,813–12,837. https://doi.org/10.5194/acp-11-12813-2011

Peischl, J., Karion, A., Sweeney, C., Kort, E. A., Smith, M. L., Brandt, A. R., et al. (2016). Quantifying atmospheric methane emissions from oil and natural gas production in the Bakken shale region of North Dakota. *Journal of Geophysical Research: Atmospheres*, *121*(10), 6101–6111. https://doi.org/10.1002/2015JD024631

Peischl, J., Ryerson, T. B., Aikin, K. C., de Gouw, J. A., Gilman, J. B., Holloway, J. S., et al. (2015). Quantifying atmospheric methane emissions from the Haynesville, Fayetteville, and northeastern Marcellus shale gas production regions. *Journal of Geophysical Research-Atmospheres*, *120*, 2119–2139. https://doi.org/10.1002/2014JD022697

Pétron, G., Karion, A., Sweeney, C., Miller, B. R., Montzka, S. A., Frost, G. J., et al. (2014). A new look at methane and nonmethane hydrocarbon emissions from oil and natural gas operations in the Colorado Denver-Julesburg Basin. *Journal of Geophysical Research: Atmospheres*, *119*, 6836–6852. https://doi.org/10.1002/2013JD021272

Pollmann, J., Helmig, D., Hueber, J., Plass-Duelmer, C., & Tans, P. (2008). Sampling, storage, and analysis of C2–C7 non-methane hydrocarbons from the US National Oceanic and Atmospheric Administration cooperative air sampling network glass flasks. *Journal of Chromatography*, *1188*(2), 75–87. https://doi.org/10.1016/j.chroma.2008.02.059

Pope, R. J., Richards, N. A. D., Chipperfield, M. P., Moore, D. P., Monks, S. A., Arnold, S. R., et al. (2016). Intercomparison and evaluation of satellite peroxyacetyl nitrate observations in the upper troposphere–lower stratosphere. *Atmospheric Chemistry and Physics*, *16*(21), 13541–13559. https://doi.org/10.5194/acp-16-13541-2016

Rap, A., Richards, N. A. D., Forster, P. M., Monks, S. A., Arnold, S. R., & Chipperfield, M. (2015). Satellite constraint on the tropospheric ozone radiative effect. *Geophysical Research Letters*, *42*(12), 5074–5081. https://doi.org/10.1002/2015GL064037

Richards, N. A. D., Arnold, S. R., Chipperfield, M. P., Miles, G., Rap, A., Siddans, R., et al. (2013). The Mediterranean summertime ozone maximum: Global emission sensitivities and radiative impacts. *Atmospheric Chemistry and Physics*, *13*(5), 2331–2345. https://doi.org/10.5194/acp-13-2331-2013

Rigby, M., Montzka, S. A., Prinn, R. G., White, J. W. C., Young, D., O'Doherty, S., et al. (2017). Role of atmospheric oxidation in recent methane growth. *Proceedings of the National Academy of Sciences*, *114*(21), 5373–5377. https://doi.org/10.1073/pnas.1616426114

Rigby, M., Prinn, R. G., Fraser, P. J., Simmonds, P. G., Langenfelds, R. L., Huang, J., et al. (2008). Renewed growth of atmospheric methane. *Geophysical Research Letters*, *35*, L22805. https://doi.org/10.1029/2008GL036037

Rudolph, J. (1995). The tropospheric distribution and budget of ethane. *Journal of Geophysical Research*, *100*(D6), 11,369–11,381. https://doi.org/10.1029/95JD00693

Rudolph, J., & Ehhalt, D. H. (1981). Measurements of C2–C5 hydrocarbons over the North Atlantic. *Journal of Geophysical Research*, *86*(C12), 11959–11,964. https://doi.org/10.1029/JC086iC12p11959

Sander, S. P., Abbatt, J., Barker, J. R., Burkholder, J. B., Friedl, R. R., Golden, D. M., et al. (2011). Chemical kinetics and photochemical data for use in atmospheric studies, Evaluation No. 17. JPL Publication 10-6. Pasadena, CA: Jet Propulsion Laboratory. Retrieved from http://jpldataeval.jpl.nasa.gov.

Schaefer, H., Mikaloff Fletcher, S. E., Veidt, C., Lassey, K. R., Brailsford, G. W., Bromley, T., et al. (2016). A 21st century shift from fossil-fuel to biogenic methane emissions indicated by $^{13}CH_4$. *Science*, *352*(6281), 80–84. https://doi.org/10.1126/science.aad2705

Schultz, M. G., Akimoto, H., Bottenheim, J., Buchmann, B., Galbally, I. E., Gilge, S., et al. (2015). The global atmosphere watch reactive gases measurement network. *Elementa science of the Anthropocene*, *3*, 67. https://doi.org/10.12952/journal.elementa.000067

Scott, C. E., Monks, S. A., Spracklen, D. V., Arnold, S. R., Forster, P. M., Rap, A., et al. (2018). Impact on short-lived climate forcers increases projected warming due to deforestation. *Nature Communications*, *9*. https://doi.org/10.1038/s41467-017-02412-4

Simpson, I. J., Andersen, M. P. S., Meinardi, S., Bruhwiler, L., Blake, N. J., Helmig, D., et al. (2012). Long-term decline of global atmospheric ethane concentrations and implications for methane. *Nature*, *488*(7412), 490–494. https://doi.org/10.1038/nature11342

Simpson, I. J., Blake, N. J., Barletta, B., Diskin, G. S., Fuelberg, H. E., Gorham, K., et al. (2010). Characterization of trace gases measured over Alberta oil sands mining operations: 76 speciated C2–C10 volatile organic compounds (VOCs), CO_2, CH_4, CO, NO, NO_2, NO_y, O_3 and SO_2. *Atmospheric Chemistry and Physics*, *10*(23), 11,931–11,954. https://doi.org/10.5194/acp-10-11931-2010

Singh, H. B. (1987). Reactive nitrogen in the troposphere. *Environmental Science & Technology*, *21*(4), 320–327. https://doi.org/10.1021/es00158a001

Sitch, S., Cox, P. M., Collins, W. J., & Huntingford, C. (2007). Indirect radiative forcing of climate change through ozone effects on the land-carbon sink. *Nature*, *448*(7155), 791–794. https://doi.org/10.1038/nature06059

Smith, M. L., Kort, E. A., Karion, A., Sweeney, C., Herndon, S. C., & Yacovitch, T. I. (2015). Airborne ethane observations in the Barnett shale: Quantification of ethane flux and attribution of methane emissions. *Environmental Science & Technology*, *49*(13), 8158–8166. https://doi.org/10.1021/acs.est.5b00219

Spivakovsky, C. M., Logan, J. A., Montzka, S. A., Balkanski, Y. J., Foreman-Fowler, M., Jones, D. B. A., et al. (2000). Three-dimensional climatological distribution of tropospheric OH: Update and evaluation. *Journal of Geophysical Research*, *105*(D7), 8931–8980. https://doi.org/10.1029/1999JD901006

Sussmann, R., Forster, F., Rettinger, M., & Bousquet, P. (2012). Renewed methane increase for five years (2007–2011) observed by solar FTIR spectrometry. *Atmospheric Chemistry and Physics*, *12*(11), 4885–4891. https://doi.org/10.5194/acp-12-4885-2012

Swarthout, R. F., Russo, R. S., Zhou, Y., Hart, A. H., & Sive, B. C. (2013). Volatile organic compound distributions during the NACHTT campaign at the boulder atmospheric observatory: Influence of urban and natural gas sources. *Journal of Geophysical Research: Atmospheres*, *118*, 10,614–10,637. https://doi.org/10.1002/jgrd.50722

Thompson, R. L., Ishijima, K., Saikawa, E., Corazza, M., Karstens, U., Patra, P. K., et al. (2014). TransCom N_2O model inter-comparison—Part 2: Atmospheric inversion estimates of N_2O emissions. *Atmospheric Chemistry and Physics*, *14*(12), 6177–6194. https://doi.org/10.5194/acp-14-6177-2014

Tilmes, S., Lamarque, J.-F., Emmons, L. K., Kinnison, D. E., Marsh, D., Garcia, R. R., et al. (2016). Representation of the community Earth system model (CESM1) CAM4-Chem within the chemistry-climate model initiative (CCMI). *Geoscientific Model Development*, *9*(5), 1853–1890. https://doi.org/10.5194/gmd-9-1853-2016

Turner, A. J., Frankenberg, C., Wennberg, P. O., & Jacob, D. J. (2017). Ambiguity in the causes for decadal trends in atmospheric methane and hydroxyl. *PNAS*, *114*(21), 5367–5372. https://doi.org/10.1073/pnas.1616020114

Turner, A. J., Jacob, D. J., Benmergui, J., Wofsy, S. C., Maasakkers, J. D., Butz, A., et al. (2016). A large increase in U.S. methane emissions over the past decade inferred from satellite data and surface observations. *Geophysical Research Letters*, *43*, 2218–2224. https://doi.org/10.1002/2016GL067987

Tzompa-Sosa, Z. A., Mahieu, E., Franco, B., Keller, C. A., Turner, A. J., Helmig, D., et al. (2017). Revisiting global fossil fuel and biofuel emissions of ethane. *Journal of Geophysical Research-Atmospheres*, *122*, 2493–2512. https://doi.org/10.1002/2016JD025767

Van Dingenen, R., Dentener, F. J., Raes, F., Krol, M. C., Emberson, L., & Cofala, J. (2009). The global impact of ozone on agricultural crop yields under current and future air quality legislation. *Atmospheric Environment*, *43*(3), 604–618. https://doi.org/10.1016/j.atmosenv.2008.10.033

Vinciguerra, T., Yao, S., Dadzie, J., Chittams, A., Deskins, T., Ehrman, S., & Dickerson, R. R. (2015). Regional air quality impacts of hydraulic fracturing and shale natural gas activity: Evidence from ambient VOC observations. *Atmospheric Environment*, *110*, 144–150. https://doi.org/10.1016/j.atmosenv.2015.03.056

Voulgarakis, A., Naik, V., Lamarque, J.-F., Shindell, D. T., Young, P. J., Prather, M. J., et al. (2013). Analysis of present day and future OH and methane lifetime in the ACCMIP simulations. *Atmospheric Chemistry and Physics*, *13*(5), 2563–2587. https://doi.org/10.5194/acp-13-2563-2013

Warneke, C., Geiger, F., Edwards, P. M., Dube, W., Pétron, G., Kofler, J., et al. (2014). Volatile organic compound emissions from the oil and natural gas industry in the Uintah Basin, Utah: Oil and gas well pad emissions compared to ambient air composition. *Atmospheric Chemistry and Physics*, *14*(20), 10,977–10,988. https://doi.org/10.5194/acp-14-10977-2014

Wiedinmyer, C., Akagi, S. K., Yokelson, R. J., Emmons, L. K., Al-Saadi, J. A., Orlando, J. J., & Soja, A. J. (2011). The fire INventory from NCAR (FINN): A high resolution global model to estimate the emissions from open burning. *Geoscientific Model Development*, *4*(3), 625–641. https://doi.org/10.5194/gmd-4-625-2011

Wilson, C., Chipperfield, M. P., Gloor, M., & Chevallier, F. (2014). Development of a variational flux inversion system (INVICAT v1.0) using the TOMCAT chemical transport model. *Geoscientific Model Development*, *7*(5), 2485–2500. https://doi.org/10.5194/gmd-7-2485-2014

Wilson, C., Gloor, M., Gatti, L. V., Miller, J. B., Monks, S. A., McNorton, J., et al. (2016). Contribution of regional sources to atmospheric methane over the Amazon Basin in 2010 and 2011. *Global Biogeochemical Cycles*, *30*, 400–420. https://doi.org/10.1002/2015GB005300

Worden, J. R., Bloom, A. A., Pandey, S., Jiang, Z., Worden, H. M., Walker, T. W., et al. (2017). Reduced biomass burning emissions reconcile conflicting estimates of the post-2006 atmospheric methane budget. *Nature Communications*, *8*(1), 2227. https://doi.org/10.1038/s41467-017-02246-0

Xiao, Y., Jacob, D. J., Wang, J. S., Logan, J. A., Palmer, P. I., Suntharalingam, P., et al. (2004). Constraints on Asian and European sources of methane from CH_4-C_2H_6-CO correlations in Asian outflow. *Journal of Geophysical Research*, *109*, D15S16. https://doi.org/10.1029/2003JD004475

Xiao, Y., Logan, J. A., Jacob, D. J., Hudman, R. C., Yantosca, R., & Blake, D. R. (2008). Global budget of ethane and regional constraints on U.S. sources. *Journal of Geophysical Research*, *113*, D21306. https://doi.org/10.1029/2007JD009415

Yacovitch, T. I., Herndon, S. C., Roscioli, J. R., Floerchinger, C., McGovern, R. M., Agnese, M., et al. (2014). Demonstration of an ethane spectrometer for methane source identification. *Environmental Science & Technology*, *48*(14), 8028–8034. https://doi.org/10.1021/es501475q

Yuan, B., Kaser, L., Karl, T., Graus, M., Peischl, J., Campos, T. L., et al. (2015). Airborne flux measurements of methane and volatile organic compounds over the Haynesville and Marcellus shale gas production regions. *Journal of Geophysical Research: Atmospheres*, *120*(12), 6271–6289. https://doi.org/10.1002/2015JD023242